

R95-970281-4

AFOSR-TR-96

0125

# ADVANCED MoSi<sub>2</sub> COMPOSITIONS

Prepared by

S. Chin  
D. L. Anton  
A. F. Giamei

FINAL TECHNICAL REPORT

Contract F49620-92-C-0043

for

Air Force Office of Scientific Research  
Building 410  
Bolling Air Force Base  
Washington, DC 20332

February 16, 1996

19960320 083

DISTRIBUTION STATEMENT A

Approved for public release  
Distribution Unlimited



**UNITED  
TECHNOLOGIES  
RESEARCH  
CENTER**

East Hartford, Connecticut 06108

DTIC QUALITY INSPECTED 1

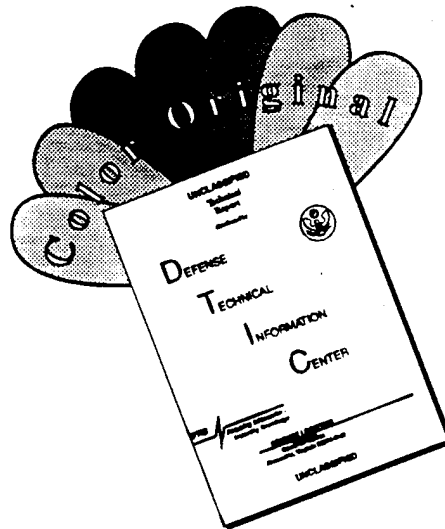
# REPORT DOCUMENTATION PAGE

Form Approved  
OMB No. 0704-0188

Public reporting burden for this collection of information is estimated to average 1 hour per response, including the time for reviewing instructions, searching existing data sources, gathering and maintaining the data needed, and completing and reviewing the collection of information. Send comments regarding this burden estimate or any other aspect of this collection of information, including suggestions for reducing this burden, to Washington Headquarters Services, Directorate for Information Operations and Reports, 1215 Jefferson Davis Highway, Suite 1204, Arlington, VA 22202-4302, and to the Office of Management and Budget, Paperwork Reduction Project (0704-0188), Washington, DC 20503.

1. AGENCY USE ONLY (Leave blank)		2. REPORT DATE <b>16 February 1996</b>		3. REPORT TYPE AND DATES COVERED <b>Final Technical Report 7/15/92 - 12/14/95</b>	
4. TITLE AND SUBTITLE <b>ADVANCED MoSi<sub>2</sub> COMPOSITIONS</b> (u)				5. FUNDING NUMBERS <b>F49620-92-C-0043</b>	
6. AUTHOR(S) <b>S. Chin, D. L. Anton, A. F. Giamei</b>					
7. PERFORMING ORGANIZATION NAME(S) AND ADDRESS(ES) <b>United Technologies Research Center 411 Silver Lane East Hartford, CT 06108</b>				8. PERFORMING ORGANIZATION REPORT NUMBER <b>R95-970281-4</b>	
9. SPONSORING/MONITORING AGENCY NAME(S) AND ADDRESS(ES) <b>USAF, AFMC Air Force Office of Scientific Research, Bldg 410 Bolling Air Force Base Washington, DC 20332</b>				10. SPONSORING/MONITORING AGENCY REPORT NUMBER	
11. SUPPLEMENTARY NOTES					
12a. DISTRIBUTION / AVAILABILITY STATEMENT <b>APPROVED FOR PUBLIC RELEASE; DISTRIBUTION UNLIMITED.</b>				12b. DISTRIBUTION CODE	
13. ABSTRACT (Maximum 200 words)  Single-phase and two-phase MoSi <sub>2</sub> and MoSi <sub>2</sub> alloys modified with Al, B, Ge, Hf, Nb and Re have been investigated. B and Hf were found to exhibit no appreciable solubility in MoSi <sub>2</sub> and were not considered for further evaluation. Alloys with Al & Nb substitutions for Si and Mo, respectively, have the hexagonal C40 crystal structure. Alloys with Ge and Re substitutions for Si and Mo, respectively, maintained the tetragonal C11 <sub>b</sub> crystal structure. Two-phase alloys modified with Nb and exhibiting the C40 + C11 <sub>b</sub> crystal structure were also evaluated. Additionally, MoSi <sub>2</sub> with the C40 structure containing Nb+Re were evaluated. The mechanical properties were evaluated using the following tests: four-point flexure testing to determine strength, ductility, modulus, and ductile-to-brittle transition temperature (DBTT); three-point notched K <sub>IC</sub> flexure testing to determine fracture toughness; compression testing to determine compressive yield strength, and compressive creep testing. Flexural testing indicate a DBTT of 1250-1350°C for the baseline MoSi <sub>2</sub> and all of the modifications evaluated. Several of the Nb and/or Re modified alloys were found to exhibit a good combination of mechanical properties. The oxidation resistance of MoSi <sub>2</sub> was not significantly altered with all of the alloy modifications evaluated. Various atomic modeling tools were evaluated to visualize bonding in MoSi <sub>2</sub> .					
14. SUBJECT TERMS <b>molybdenum disilicide, molybdenum disilicide alloys, intermetallics, C11<sub>b</sub> and C40 crystal structures, mechanical properties, compression testing, ductile-to-brittle transition temperature, DBTT, arc-melting, oxidation resistance, atomic modeling, charge density, bonding, LKKR, LASTO</b>				15. NUMBER OF PAGES <b>81</b>	
				16. PRICE CODE	
17. SECURITY CLASSIFICATION OF REPORT <b>Unclassified</b>	18. SECURITY CLASSIFICATION OF THIS PAGE <b>Unclassified</b>	19. SECURITY CLASSIFICATION OF ABSTRACT <b>Unclassified</b>	20. LIMITATION OF ABSTRACT <b>None</b>		

# DISCLAIMER NOTICE



THIS DOCUMENT IS BEST QUALITY AVAILABLE. THE COPY FURNISHED TO DTIC CONTAINED A SIGNIFICANT NUMBER OF COLOR PAGES WHICH DO NOT REPRODUCE LEGIBLY ON BLACK AND WHITE MICROFICHE.

## TABLE OF CONTENTS

1.	INTRODUCTION .....	1
1.1	Advanced Gas Turbine Requirrements.....	1
1.2	Materials Considerations.....	1
1.3	MoSi <sub>2</sub> Background.....	2
2.	ALLOY SELECTION .....	5
2.1	Approach.....	5
2.2	Alloy Theory.....	5
2.3	Atomic Modeling.....	7
3.	EXPERIMENTAL PROCEDURE .....	14
3.1	Alloy Casting and Homogenization Heat Treatment.....	14
3.2	Mechanical Test Specimen Preparation.....	14
3.3	Characterization.....	15
3.4	Mechanical Testing.....	15
4.	RESULTS AND DISCUSSION .....	17
4.1	Phase I Alloy Screening.....	17
4.1.1	Alumium Modifications.....	17
4.1.2	Boron Modifications.....	17
4.1.3	Germanium Modifications.....	18
4.1.4	Hafnium Modifications.....	18
4.1.5	Niobium Modifications.....	18
4.1.6	Rhenium Modifications.....	18
4.2	Phase I Property Evaluation.....	19
4.2.1	Mechanical Properties.....	19
4.2.2	Oxidation Resistance.....	19
4.3	Phase II Alloy Screening.....	19
4.3.1	Alumium Modifications.....	20
4.3.2	Germanium Modifications.....	20
4.3.3	Niobium Modifications.....	20
4.3.4	Rhenium Modifications.....	20
4.4	Phase II Property Evaluation.....	20
4.4.1	Mechanical Properties.....	20
4.4.1.1	Four-Point Flexural Testing.....	20
4.4.1.2	Three-Point Flexural K <sub>IC</sub> Testing.....	21
4.4.1.3	Compression Testing.....	21
4.4.1.4	Compressive Creep Testing.....	21

4.5	Phase III Alloy Screening.....	22
4.5.1	Niobium Modifications.....	22
4.5.2	Rhenium Modifications.....	23
4.5.3	Niobium and Rhenium Modifications.....	23
4.6	Phase III Property Evaluation.....	23
4.6.1	Mechanical Properties.....	23
4.6.1.1	Four-Point Flexural Testing.....	23
4.6.1.2	Three-Point Flexural $K_{IC}$ Testing.....	23
4.6.1.3	Compression Testing.....	24
4.6.1.4	Compressive Creep Testing.....	24
4.6.2	Oxidation Resistance.....	24
4.7	Atomic Modeling.....	25
5.	CONCLUSIONS .....	27
6.	REFERENCES .....	29
7.	TABLES .....	31
8.	FIGURES .....	52

## **1. INTRODUCTION**

### **1.1 Advanced Gas Turbine Requirements**

The performance of the next generation of military gas turbine engines will be largely determined by the temperature capabilities of structural materials. This is especially true in the case of the high pressure turbine where gas path temperatures already approach 1800°C and metal temperatures approach 1150°C. Programs such as the DoD IHPTET initiative are aimed at doubling the thrust-to-weight performance of military engines. To accomplish this objective, design calculations indicate that gas path temperatures of about 2100°C are required. The same goal can be accomplished utilizing advanced cooling schemes (possible with conductive materials such as metals and intermetallics) that maintain a gas path temperature of 2100°C and a metal temperature of 1540°C. These temperature requirements are clearly beyond the capabilities of materials currently available. In addition to the temperature requirements, other critical materials properties cannot be compromised. These properties include environmental resistance (oxidation and hot corrosion), adequate low temperature fracture toughness or ductility, elevated temperature strength (tensile and creep), and thermal-mechanical fatigue resistance.

### **1.2 Materials Considerations**

The materials used exclusively in the high pressure turbine of all state-of-the-art military engines are nickel-based superalloys. These materials are unique in that they exhibit sufficient mechanical properties and environmental resistance to be used at temperatures up to about 85% of the absolute melting point. This enhanced capability, relative to other alloy systems, can be attributed to the use of coherent precipitation strengthening, alloy modifications with rhenium additions for enhanced creep resistance and technologies such as directional solidification for enhanced thermal fatigue resistance. Since the melting points of these alloys are about 1350°C, close to that of pure nickel, significant further advancements in temperature capability will not be attainable.

Several classes of materials can potentially meet the aggressive goals stated above. They include ceramics and ceramic matrix composites (CMCs), refractory metals with protective coatings, and intermetallics and intermetallic matrix composites (IMCs). However, all of these materials will require major improvements in one or more critical properties to attain the required blend of environmental resistance, low temperature ductility (or toughness) and high temperature strength.

In general, the ceramics and CMCs suffer from a lack of ductility and fracture toughness throughout the temperature range. Additionally, their low thermal conductivity would have a negative impact on the ability to utilize advanced cooling schemes. They have the advantage of low densities and good oxidation resistance. The shortcoming of available refractory metals is poor oxidation resistance. Although they can be improved with protective coatings

(such as plasma sprayed MoSi<sub>2</sub> coatings or diffusion slurry silicide coatings for niobium alloys), failure of these coatings results in rapid deterioration of the substrate due to either internal oxidation (resulting in alloy embrittlement) or non-protective oxidation. Refractory metals have the advantages of having a mature metallurgical knowledge and experience base, good thermal conductivities, adequate ductility throughout the temperature range of interest, and can be strengthened by traditional solid solution and dispersion hardening techniques<sup>1</sup>. Intermetallics generally exhibit insufficient ductility at low temperatures (below the alloy ductile-to-brittle transition temperature [DBTT]) and inadequate strength at elevated temperatures. They have good thermal conductivities such that advanced cooling schemes can be used and they have lower densities than the refractory metals (but generally higher than the ceramic materials). Several of the intermetallic systems such as NiAl and MoSi<sub>2</sub> exhibit excellent oxidation resistances. Of all the intermetallics, MoSi<sub>2</sub> has the best combination of a high melting point, high temperature strength, and oxidation resistance.

### 1.3 MoSi<sub>2</sub> Background

The properties of MoSi<sub>2</sub> have been investigated for potential applications as a high temperature structural material, furnace heating elements, protective coatings for refractory metals, and thin film diffusion barriers at interconnects in semiconductor devices. The properties of interest for potential application in advanced gas turbine engines are (1) elevated temperature oxidation resistance (2) intermediate temperature oxidation resistance (3) high temperature strength (including creep) (4) brittle-to-ductile transition and (5) low temperature fracture toughness.

The acceptance of MoSi<sub>2</sub> as a high temperature material is primarily attributable to its excellent oxidation resistance. It is the material of choice as heating elements for air furnace applications to temperatures slightly in excess of 1800°C. This remarkable protection is due to the ability of the material to form a pure SiO<sub>2</sub> scale. Excellent oxidation resistance is attained because of three factors. First, the free energy of formation for SiO<sub>2</sub> is significantly lower than for MoO<sub>3</sub> and favors SiO<sub>2</sub> formation. Second, MoO<sub>3</sub> has a very high vapor pressure and at temperatures above about 800°C, will evaporate and leave behind a pure SiO<sub>2</sub> scale. Third, the growth rate of the SiO<sub>2</sub> scale is very slow. The parabolic rate constants (a measure of scale growth rate) shown in Fig. 1 indicate a SiO<sub>2</sub> scale grows more slowly than a Al<sub>2</sub>O<sub>3</sub> scale at temperatures above about 1500°C. The oxidation resistance of MoSi<sub>2</sub> at intermediate temperatures is of some concern. At temperatures ranging from 500 to 600°C, a phenomenon called "pestring" has been observed. This phrase was first referenced by Fitzer<sup>2</sup> and is generally defined as the disintegration of a material after cyclic exposure to intermediate temperatures. More recent work on MoSi<sub>2</sub> by most investigators have not indicated a pestring problem. This suggests that the problem is associated with the processing and/or purity of early material. This was confirmed by Meier<sup>3</sup>, who observed pestring in arc-melted and porous P/M MoSi<sub>2</sub> after exposures at 500°C.

The mechanical properties of monolithic MoSi<sub>2</sub> indicate the material, in pure form, exhibits inadequate ductility or fracture toughness at low temperatures and insufficient strength at elevated temperatures. The properties can be characterized by three different performance regions<sup>4</sup>. At low temperatures (below the DBTT of about 1000°C), MoSi<sub>2</sub> is strong and brittle. At intermediate temperatures (above the 1000°C to about 1250°C) MoSi<sub>2</sub> is strong and ductile. At elevated temperatures (above about 1250°C), MoSi<sub>2</sub> is ductile but exhibits low strength. The ultimate strength of pure MoSi<sub>2</sub> has been determined by various investigators and is constant at 280-350 MPa from low temperatures to about 1250°C as shown in Fig. 2. Above this temperature, the strength decreases rapidly (due to thermally activated processes). This strength level is lower than that of cobalt and nickel-based superalloys at low temperatures where strengths of about 500 to 1000 MPa is required for highly stressed components such as turbine blades and vanes. At temperatures above 1100°C when the strength of the cobalt and nickel alloys decreases rapidly as we approach their melting points, the MoSi<sub>2</sub> exhibits higher strengths. Similarly, MoSi<sub>2</sub> exhibits greater creep resistance above 1100°C as shown by the results in Fig. 3. The fracture toughness of MoSi<sub>2</sub> is only about 2 MPa·√m which is typical of most intermetallic and ceramic materials. These mechanical property results certainly indicate a need to improve the low temperature fracture toughness and elevated temperature mechanical properties of MoSi<sub>2</sub>.

Only limited investigations have been found which dealt with improving the mechanical properties of MoSi<sub>2</sub> through alloying. Researchers<sup>5</sup> have found that the addition of germanium to MoSi<sub>2</sub> improves the cyclic oxidation resistance of MoSi<sub>2</sub> and is especially effective in minimizing peeling. Altering the viscosity and coefficient of thermal expansion of the SiO<sub>2</sub> scale results from germanium additions. This minimizes thermal stresses between the alloy and the oxide scale, reducing scale cracking and spallation. To improve the performance of heating elements, Kanthal Corp. alloys MoSi<sub>2</sub> with significant levels of tungsten. An examination of the Mo-W-Si ternary phase diagram indicates that alloying with about 50 atom percent tungsten for molybdenum would improve the melting point and the high temperature capabilities of MoSi<sub>2</sub> by about 70°C (thus extending the use temperature to about 1900°C). In work performed at UTRC that was internally funded and subsequently sponsored by WRDC<sup>6</sup>, rhenium modifications were found to significantly reduce the minimum creep rate of MoSi<sub>2</sub>. The results in Fig. 4 indicate the minimum creep rate for rhenium modified MoSi<sub>2</sub> exhibits one to two orders of magnitude lower creep rate than unalloyed MoSi<sub>2</sub> at 1000°C and at 1400°C. In this same study, tungsten was found to have little effect on elevated temperature creep strength. An understanding of these compositional effects has not been established.

Intermetallic matrix composites based on MoSi<sub>2</sub> are being investigated to meet the requirements of the next generation gas turbine engines. The objectives of these investigators are the same as ours, that is, to improve the low temperature fracture toughness and elevated temperature strength of MoSi<sub>2</sub>. Most of the work is currently centered on the fabrication of MoSi<sub>2</sub> based intermetallics and on the effect and compatibility of different reinforcing fibers. The SiC whisker/MoSi<sub>2</sub> matrix composite system has attracted the most interest. This is



attributed to the availability of the reinforcements and to the oxidation resistance and thermal stability of the SiC with respect to MoSi<sub>2</sub>. The results of the various studies indicate only modest improvements in strength and fracture toughness were attained. For example, the fracture toughness of MoSi<sub>2</sub> was improved<sup>7</sup> from 2 to only about 5 MPa·√m. Similarly, only a marginal improvement in elevated temperature strength was observed. The greatest increases in fracture toughness have been obtained utilizing refractory metal fibers. For example, fracture toughnesses of up to 39 MPa·√m have been achieved<sup>8</sup>. Unfortunately, refractory metal fibers are not thermodynamically stable with respect to MoSi<sub>2</sub> and either dissolve (and alloy with MoSi<sub>2</sub> to form a lower silicide) or react to form a more stable silicide such as NbSi<sub>2</sub>. Additionally, any exposed refractory metal fibers will compromise the oxidation resistance of MoSi<sub>2</sub>. The current work on alloy matrix composites have been concentrated in the (W-Mo)Si<sub>2</sub> matrix/SiC fiber system. As expected, only modest improvements in strength and fracture toughness have been achieved using this alloy matrix.

These results indicate MoSi<sub>2</sub> offers excellent oxidation resistance along with the potential for high temperature strengthening through compositing and matrix alloying. With respect to alloying, little has been done to investigate compositional effects on the mechanical properties of MoSi<sub>2</sub>. This program is aimed at improving and understanding the mechanical properties of MoSi<sub>2</sub> through compositional modifications and towards the understanding and development of materials having the balanced properties needed in the next generation gas turbine engines.

## 2. ALLOY SELECTION

### 2.1 Approach

In this program, the compositional effects on the mechanical properties of  $\text{MoSi}_2$  are being investigated. The objective of this activity is to predict, study and reconcile alloying effects on the elevated temperature strength and low temperature fracture toughness. The approach used is to select appropriate alloying elements based on state-of-the-art alloy design theory. After suitable alloys have been identified, materials fabrication for evaluation is accomplished by appropriate arc-melting, powder metallurgy (including vacuum hot pressing or hot isostatic pressing) and plasma spraying techniques which have already been developed for preparation of intermetallic alloys. The phase stability, structure, and mechanical properties are being measured, correlated with predicted effects and compared to the baseline  $\text{MoSi}_2$  properties.

The significance of this work is not restricted to achieving a fundamental understanding of alloying effects on  $\text{MoSi}_2$ , but will also be realized when used in conjunction with the best compositing techniques being evaluated by other investigators. It is viewed that this program would complement the composite effort on improving low temperature fracture toughness and elevated temperature strength. Both of these efforts are necessary to achieve the goal of developing suitable materials for the next generation gas turbine engines.

### 2.2 Alloy Theory

The selection of alloying elements for evaluation is based on the best available phase equilibria, alloy theory, simulation or modeling capabilities, and property requirements. Phase equilibria and crystal structures in the Mo-Si-X ternary system is of primary importance. Elemental additions that compromise the melting point (by forming lower melting silicides) were not selected. Since most structural materials are usable to about  $0.5-0.6T_m$ , any significant reduction in the melting point of  $\text{MoSi}_2$  ( $2020^\circ\text{C}$ ) is undesirable. Based on this criterion, the best elemental candidates are tungsten, rhenium, tantalum, niobium, germanium and carbon. The solubility limits of ternary alloying additions into  $\text{MoSi}_2$  are not well documented and while a number of these diagrams are published, there are numerous inconsistencies and errors. For example, the ternary Cr-Mo-Si phase diagram<sup>9</sup> shown in Fig. 5 indicates a large  $\text{MoSi}_2$  phase field with the  $\text{C11}_b$  crystal structure but internal work at UTRC indicates this solubility range only extends to about 2 weight percent chromium. More detailed ternary phase diagrams are being made of each alloy system studied.

The crystal structure of a material has a significant effect on the mechanical properties. Differences in the crystal structure will have significant impact on the number of slip systems available and the operative slip vectors. In addition to solid solution alloying, additions will be selected to stabilize specific crystal structures in the  $\text{MoSi}_2$  system. The equilibrium structure for  $\text{MoSi}_2$  is the  $\text{C11}_b$  tetragonal phase. There is currently a controversy as to the existence of a stable  $\text{C40}$  hexagonal structure in the  $\text{MoSi}_2$  system. This structure is either a

metastable phase<sup>10</sup> or a high temperature phase<sup>11</sup> (occurring above 1900°C). Interstitial elements such as carbon are believed to stabilize the C40 phase and research is being conducted in this area<sup>12</sup>.

Engel-Brewer diagrams<sup>13</sup> provide a perspective on the nature of crystal structure similarities which are not evident from crystallographic data; such data consists primarily of symmetry elements and overlooks relative differences in structure. The strength of these diagrams over other mapping schemes is that the solubility limits of compounds and solid solutions are readily apparent as a function of ternary alloying. These maps are simply composites of binary phase diagrams taken at one temperature. An examination of such a map with silicon indicates the C11<sub>b</sub> structure is stable for Mo, W, and Re. One notes that disilicides with lower electron/atom ratios than MoSi<sub>2</sub> (C11<sub>b</sub>) have the C40 structure. The C40 structure is simply a shear vector removed from the C11<sub>b</sub> structure<sup>13</sup>. Other closely related structures such as C54 and C49 have also been identified. While both Engel-Brewer and Pettifor<sup>14</sup> maps would indicate that the C40, C49, and C54 crystal structures are closely related to that of C11<sub>b</sub>, the actual geometric relationship has only been obtained for the C40 structure. These relationships have not been explored in great detail and simply detailing the atomic motions required for the transformations will be a significant task.

Having isolated the structural similarities, partial destabilization of the C11<sub>b</sub> structure can lead to coherent precipitation or enhanced ternary solubility which could lead to greater creep resistance while a lowered ordering parameter may result in a lowered DBTT and enhanced low temperature ductility. An example of the destabilization of the C11<sub>b</sub> structure leading to enhanced ternary solubility occurs in the case of chromium additions to MoSi<sub>2</sub>. CrSi<sub>2</sub> has the C40 structure and is expected to partially destabilize C11<sub>b</sub> towards the C40 structure. Examination of this phase diagram would indicate that the MoSi<sub>2</sub> phase field can be expanded considerably in ternary space. This is attributed to chromium substitution for either molybdenum or silicon in MoSi<sub>2</sub> while molybdenum substitutes only for chromium in CrSi<sub>2</sub>. The effect on strength of MoSi<sub>2</sub> through chromium additions has been recently documented<sup>15</sup>. It is expected that other such alloying approaches can be used to strengthen MoSi<sub>2</sub>.

Similarly, titanium is expected to stabilize the C54 structure (TiSi<sub>2</sub>) while zirconium or hafnium is expected to stabilize the C49 structure (ZrSi<sub>2</sub> and HfSi<sub>2</sub>), and their additions are being considered.

With respect to major alloying modifications, the two methods most cited in the literature<sup>16,17</sup> as being responsible for altering the crystal structure and properties of intermetallic compounds are (1) electron-to-atom ratios (e/a) of the compounds<sup>16,18</sup> and (2) relative atomic radii ratios ( $R_a/R_b$ ) of the compounds<sup>17,19</sup>. These are accomplished through substitutional alloying. The e/a ratio modifications are accomplished by substituting elements into MoSi<sub>2</sub> which are expected to maintain single phase compounds but which contain either an excess or deficit of electrons with respect to the substituted element. Determination of electron densities per atom is done by counting the average electrons per atom in excess of the inert

gas core electrons. This has been shown to be an adequate measure of electron density<sup>20</sup>. For example, substitution of rhenium for 25 atomic percent molybdenum would increase the  $e/a$  from 4.67 to 4.75. Similarly, substitution of niobium for molybdenum would decrease the  $e/a$  from 4.67 to 4.58.

Atomic radii ratio modifications are accomplished in a similar way but with the  $e/a$  ratio constant. Since the atomic radii in intermetallic compounds are not fully understood, the hard sphere approximation is being used. More suitable radii will also be sought such as ionic radii or some fraction of atomic radii which may yield results that can be correlated with the experimental findings. As an example, an alloy modification to  $\text{MoSi}_2$  to change  $R_a/R_b$  would be to substitute germanium which has an atomic radius of 0.139nm for silicon which has an atomic radius of 0.117nm.

Based on the approaches described, six elemental modifications were selected for study in the initial phase of this program. The modifications were selected based on available phase diagrams, melting temperatures, crystal structures,  $e/a$  ratios and atomic radii.

The elements selected are B, Al, Ge, Re, Nb, and Hf. Boron was selected in an attempt to stabilize the C32 structure as well as evaluating the effect of smaller atomic radii (boron has an atomic radius of 0.097nm while silicon has an atomic radius of 0.117nm). Aluminum was selected because of the large solubility range of  $\text{Mo}(\text{Si},\text{Al})_2$  which has the C40 structure. Germanium was selected because it has complete solubility in  $\text{MoSi}_2$  with the C11<sub>b</sub> structure when substituted for silicon. Germanium also has a significantly larger atomic radius (0.139nm) than silicon (0.117nm). Re was selected because of its complete solubility in  $\text{MoSi}_2$  with the C11<sub>b</sub> structure. Additionally, the melting temperature and  $e/a$  ratio are expected to increase with rhenium substitutions for molybdenum. Niobium was selected because a high solubility of Nb in  $\text{MoSi}_2$  (C11<sub>b</sub>) and Mo in  $\text{NbSi}_2$  (C40) are expected. Additionally, the  $e/a$  ratio is reduced with niobium substitutions for molybdenum. Hafnium modifications were selected to attempt to stabilize the C49 crystal structure as well as further reducing the  $e/a$  ratio with hafnium substitutions for molybdenum.

### 2.3 Atomic Modeling

Materials properties controlled at the atomic level can in principle be calculated from quantum mechanical methods. These phenomena include the ground and excited crystal structures along with their lattice parameters and enthalpies of transformation, coefficients of thermal expansion, single crystal elastic constants, Peierls' barrier, dislocation core energies, and barriers to diffusion. While there are no limitations, in principle, to the accuracy with which these calculations can be performed, there are a number of practical considerations which have complicated the uses of these techniques as metallurgical tools.

Among the most significant practical limitations are those concerned with the numerical solution of the Schroedinger Wave Equation for a large number of symmetry-unique atoms. This limitation has motivated a variety of approximate methods which are now employed to generate solutions to this equation. As the speed of digital computers has continued to increase, the severity of the approximations required has diminished. Today the ready availability of quantum mechanical software, coupled with high speed workstations makes it possible that metallurgical research can prosper from the use of quantum mechanical methods. There is also every reason to believe that as the number of investigators using these methods increases, new capabilities will be provided at a rapid pace. Some of the underlying principles of quantum mechanical methods will be summarized here in an attempt to give the average metallurgist a firmer foundation from which to appraise the usefulness of these methods in his or her research program.

To begin with, all quantum mechanical methods are involved in finding the solutions to either the Schroedinger or Dirac equation. Of the two, the Dirac equation is far more difficult to solve, but its solutions include relativistic effects experienced by electrons as they move about the nucleus. For the most part, these effects are very small, but become appreciable as the positive charge of the nucleus increases. These effects are considered to be significant for atoms heavier than Hf. While the solutions to the Schroedinger equation do not include these relativistic effects directly, corrections can be made to include many of these effects indirectly. The methods, which solve the Schroedinger equation with varying degrees of relativistic corrections, are the most common; it is those solutions and methods which will be discussed in this report.

The solution to any quantum mechanical equation, including the Schroedinger equation, gives two results. The first of these is an electronic energy, which is equivalent to the thermodynamic energy, i.e. the enthalpy, of the system at zero degrees Kelvin. This energy is generally orders of magnitude larger than vibrational and rotational energies, which become appreciable at high temperatures, and is itself nearly constant as a function of temperature. The other result of the solution to the Schroedinger equation is a wavefunction, which provides information regarding the electron distribution in the system.

As the energy resulting from a QM calculation represents an enthalpy, the changes in enthalpy associated with various structural and chemical changes can in principle be determined through quantum mechanical methods. Combined with statistical approaches, one can then deduce a change in free energy and consequently all of the thermodynamic properties of a system of interest. While the utility of the quantum mechanically calculated energy should be obvious, the practical uses of the charge density or wavefunction is more abstract. Often this information has been utilized to provide insight about the nature of the bonding present in a material or molecule. It should be emphasized, however, that the chemical bond is an abstraction for which there is no physical analog.

The single rigorous relationship between the charge density and materials properties makes use of the electrostatic theorem. This theorem states that the force exerted on a nucleus from a given charge distribution can be determined from classical electrostatics. So once a charge density of purely quantum mechanical origin has been determined, it is possible to analyze the force on the nuclei of that system from classical electrostatics. It is from this theory that much of the concept of bonding has been developed. In a molecular system where there is a buildup of charge density between atoms, the atoms are said to be bound, for, assuming that the charge density is rigid, the local density will act to hold the nuclei together as one tries to separate them.

Writing down the Schrodinger equation for a specific molecule or solid involves determining the potential acting on each electron. There are two parts to this potential: i) the attraction between the electron and each nuclei, and ii) the repulsion between the electron and all others. This latter potential, electron-electron repulsion, gives rise to the phenomenon of electron correlation, whereby electrons will move in a fashion so as to stay out of each other's way. The electron-electron repulsion also guarantees that for all systems with more than two electrons, there is no solution to the Schrodinger equation which can be represented as a simple analytical function. While it is, in principle, possible to calculate a wave function and energy for any system exactly, the solutions will always take the form of an infinite series. In practice, therefore, one must truncate these series after some number of terms, giving rise to an error in both the energy and wavefunction. There are two approaches to minimizing this error. One, is to find rapidly converging basis sets in which to expand the solutions, while the other is to use basis sets which provide some mathematical convenience allowing one to handle more terms in the expansion.

One of the more rapidly converging basis sets is that made up of the so called spherical harmonics. These functions are the familiar s, p, d, and f orbitals, the shapes of which are familiar to all freshmen chemistry students. These are, in fact, the angular part of the solutions to the central force problem, i.e. that part of the atomic Schrodinger equation which does not involve electron-electron repulsion. This being the case, it is no wonder that these functions are rapidly convergent, at least when electron correlation is ignored.

When electron correlation is included, many more spherical harmonics must be included in the expansion of the wavefunction. Including these terms is referred to as including configuration interactions or CI terms. The larger the basis set in which the solution is expanded the more computationally intense the problem. Including CI interactions rapidly increases the complexity of the problem. As such this approach is used primarily for small molecules where a high degree of accuracy is required. These approaches are referred to collectively as Hartree-Fock (HF) methods, and are distinguished by the fact that one can systematically improve the accuracy of the calculation by increasing the size of the basis set. In principle, HF methods can produce an exact answer, though in application there is always some error introduced by the limited basis set.

Another approach to solving the Schroedinger equation which can, in theory, produce an exact answer is referred to as a local-density-functional (LDF) approach. This approach make use of a theorem proved by Kohn and Sham showing that the energy of a molecular or solid state system is a functional of the electron density. The Schroedinger equation cast in the form of a density functional equation is referred to as the Kohn-Sham equation. The disadvantage in using LDF methods, is that the exact functional form by which the energy depends on the electron density is unknown. As a consequence, a number of functional forms have been suggested and are constantly being refined to produce answers which are consistent with experiment and other theories. The advantage of LDF methods is that the results are not as sensitive to basis set size, with electron correlation and exchange included in the functional. As a result, smaller basis sets are required and larger systems can be realistically treated. Just as with HF methods, LDF methods can theoretically provide exact solutions while in practice, some error is introduced: not as much by a limited basis set, but by the form of the density functional. For the most part LDF techniques have been those most commonly used to study solid state phenomena, while HF approaches have been preferred in the study of molecular properties. As LDF methods are not hampered by needing to use extremely large basis sets to treat exchange and correlation, novel methods could be used in solving Kohn-Sham equation without introducing excessive additional errors. This was particularly true in the 60 s and 70 s where even the super-computers of the day were limited in terms of the size of the problem which could be handled, even when employing the LDF approximations.

One of the novel methods most deserving of comment is that involving the partitioning of the molecular or solid state potential into a spherical part, called the muffin tin, and a constant part located between atoms in the interstitial region. For the time, this was an excellent approximation, since to an electron near an atomic nucleus "sees" primarily the central force from that nucleus, while in the interstitial region the potential is slowly varying and can be treated as constant. For a constant spherical potential, the solutions to the Schroedinger equation are in the form of a radial part (a linear combination of spherical harmonics) near the nucleus and, in the interstitial region, the solutions are in the form of plane waves. By requiring that the solutions between the two regions be smooth and continuous, one generates an acceptable solution to the molecular or solid state problem. These approaches are collectively referred to as muffin tin techniques and assume some shape for the potential. Today it is no longer necessary to assume a shape of the molecular or solid state potential and methods which do not assume a potential shape are called full potential techniques. Even though these methods make no approximations to the molecular potential they still often partition space into an atomic region and an interstitial region, separately, solving the Schroedinger equation in each region and then matching solutions across the region boundaries to produce the correct full solution.

All current full potential LDF codes are capable of producing results with similar accuracy. Using these full potential techniques along with the newest local-density-functionals, current calculations are capable of determining equilibrium lattice constants within about 2%, elastic constants to better than 15%; all of this can be done for unit cells containing as many as 15

atoms. What distinguishes one full potential approach from another is the basis set in which the solution is expanded. For example, plane wave expansions offer a number of attractive mathematical properties; consequently, there are a number of methods which make use of plane wave expansions. One of the best known of these is the FLAPW method, standing for full potential linear augmented plane wave method. Another method is the FLASTO method, which is a full potential linear augmented Slater type orbital approach. In this approach Slater type orbitals are used to expand solutions to the Schroedinger equations.

Other letters of the alphabet soup used in referring to electronic structure methods relay information regarding how a problem is solved rather than the basis set in which it is solved. For example, KKR methods are Green's function techniques which solve the Schroedinger equation as a scattering problem. Many of these techniques use the muffin tin approximation e.g. the LKKR technique.

Another advantage of full potential approaches, in addition to their superior accuracy when determining energies, is that of producing smooth charge densities and wavefunctions. Unlike muffin tin approaches, the cusps and sharp corners where the wavefunctions cross the muffin tin boundaries are not seen. For those interested in establishing correlations between variations in charge density and properties, full potential techniques should be used. All full potential techniques provide the necessary accuracy to determine a number of quantities of interest to metallurgists, what has complicated their use is that most really interesting metallurgical parameters: defects, diffusion barriers, ternary and quaternary effects, etc. can only be modeled as large supercells, or clusters, with very many symmetry unique atoms per unit cell or in the cluster. These very large systems offer their own complications, and research has proceeded along two courses.

The first of these has relied on the increasing speed of computers. Using the same algorithms that 15 years ago allowed for full potential calculations on three symmetry unique atoms per unit cell, calculations can now be performed on unit cells containing ten or fifteen symmetry unique atoms and require approximately the same amount of CPU time.

Combining increased computer speed with improved algorithms now allows the modeling of supercells with up to 50 atoms per cell. The most important improvement in computational approach comes from a set of methods known as linear methods. This is the L in FLAPW, LASTO, or LMTO. These methods are all accurate and fast. Still these approaches are not capable of modeling, for example, a dislocation core, which might require a 1000 atoms per unit cell. However, given the speed of computer processors is doubling once a year and multi-processor machines are more common-place, in time such large calculations should be practical. Therefore, researchers following this course have been involved in increasing the speed of their computations, without sacrificing accuracy, anticipating that in the not to distant future very large and meaningful problems can be handled with the techniques which can in principle provide exact solutions.



There are also some specialty codes which were designed to treat a particular class of phenomena. The LKKR is an example. This approach allows one to treat isolated coherent interfaces and has proven useful in the determining boundary energies such as SF's, APB's, and grain boundaries. This technique uses the muffin tin approximation and therefore is best suited to modeling boundaries with a minimum of free volume.

The second course of research has involved adopting approximate methods which allows one to model systems with comparatively large numbers of atoms with existing computers. An example of one such method falls under the general category of "atomistic methods". These techniques ASSUME that there is a potential of interaction between atoms. With such an assumption, it is possible to calculate dynamic effects for large ensembles of atoms, e.g. modeling crack-tips, dislocation dynamics, etc. The principal drawback for these methods is that the assumed atomic potential can only approximate atomic interactions.

When one assumes that this potential arises only between pairs of atoms, one has a so called pair potential. Pair potential techniques assume that the energy of interaction between atoms depends only on the distance between the atoms. There are numerous corrections to the simple "pair approximation". These corrections involve adding three and four body terms. The pair approximation, by itself, is equivalent to assuming that only the length or stretch of chemical bonds contributes to the energy of the system. Addition of three body terms introduces the energy of bond bending to the total energy of the system, and higher order terms introduce quadrupole effects etc.. Because these techniques are approximate, it is only possible to calibrate their accuracy against known results. As an example, pair potential techniques provide answers which are fairly good in systems where there is little directional character to the bonding. So in pure Ni, Cu, and Al the calculations are reasonable. However, in Si, W, and Ir these calculations give poor results. Thus one is confronted with the following conundrum when using approximate methods: while calculations work quite well to explain the properties of pure Al and Ni, what about NiAl? The only way to tell is to perform the experiment modeled and compare the results. But if every calculation requires an experiment, there is no advantage to the calculations.

Though some disagree, our opinion is that many of these techniques are best used to study materials properties in general rather than to seek to model specific systems. A famous example of this kind of research comes from bubble raft models. Certainly these types of models provide much insight into the dynamics of dislocations in general, but one would be hard pressed to defend the position that such models have any thing to do with dislocation dynamics in specific systems, e.g. aluminum.

There are a number of electronic structure methods which should be included as approximate techniques. The first of these is a class of electronic structure methods known as pseudo-potential methods. These techniques have proved to be very fast, accurate and capable of treating large unit cells for certain types of materials. This approach treats only the valence electrons exactly and assumes that they see a "pseudo-potential" from the core electrons. The

creation of these pseudo-potentials is a great art. Once a good pseudo-potential is constructed, accurate calculations can be performed. The materials where pseudo-potential techniques work best are metals like Al and Na, as well as semiconductors such as Si. A second approximate method developed to treat a dilute impurity is called the CPA or coherent potential approximation. Using this method one does not need to construct a huge super cell of 100 atoms to model a 1 atomic per cent impurity. The CPA is a mean field approach which assumes that an atom in a solution or alloy sees the average potential of all the other atoms. For many problems this seems to be a good approximation; for others it does not. So, just as with the pair potential techniques, because these methods are approximate there can be no certainty that the results of a calculation are predictive or simply manifestations of the approximation. In the end, all approximate methods suffer from this uncertainty.

From a metallurgical perspective the biggest barrier to the use of QM methods as practical tools is the need to treat larger cells and lower symmetry systems. One should keep in mind however, that ten years ago only those facilities with super-computers could undertake to do QM calculations on crystals having more than 4 atoms per cell. Today, software designed to run on RISC workstations can be used to calculate the electron density and energy of crystals with 8 or more atoms per cell. With this pace of advancement, it is only a matter of time before QM methods become truly useful as a metallurgical tool. In the interim, the improvement and development of these methods will be driven by metallurgists who use these tools to their present limit, and demand more flexible and useful codes. As many of the techniques are now quite robust, their use by the novice is constrained by the tedium of creating input files and analyzing the results. "Builder" tools are now available to set up a problem for analysis once the crystal structure, atomic positions and lattice parameter(s) are known. Recently a number of graphic user interfaces, sitting between the user and many of these codes, have found their way into the marketplace. What these interfaces lack is some direction for setting up metallurgically meaningful calculations. For example, the tools are presently in place which would allow one to explore the effects of ternary additions to the phase, mechanical behavior, and interfacial energies of an ordered binary alloy. The design of this series of calculations would still require an expert in the use and interpretation of electronic structure codes. However, creating the capability, within an existing GUI, which guides the user through the design of a series of calculations and helps in the analysis of the results is a feasible objective. Such a capability will only be driven by demand and without the involvement of metallurgist at this time, with the tools that exist, this demand will never be realized.

### 3. EXPERIMENTAL PROCEDURES

#### 3.1 Alloy Casting and Homogenization Heat Treatment

Intermetallic alloys for this program were prepared by arc-melting. Arc-casting was accomplished using a specially constructed, tri-electrode apparatus which was designed to accommodate batch sizes up to 150 grams. Purified argon gas, gettered by flowing standard bottled gas over heated titanium chips, was used to create a protective atmosphere which minimizes interstitial pick-up. As a measure to reduce nitrogen and oxygen impurity levels further, a titanium bar was melted in the chamber prior to melting the alloy constituents. Typical oxygen impurity levels in the argon gas, monitored continuously throughout the melting process, were below  $10^{-7}$  ppm by weight (one part impurity in  $10^{13}$  parts argon).

Buttons were cast in water-cooled copper hearths using a minimum of three melting and resolidification sequences; to minimize macroscopic homogeneity, the cast buttons were "flipped" between melting operations.

Heat treatments were performed in an all-metal tungsten-element vacuum furnace. Purified helium or argon gas, also gettered by flowing standard bottled gas over heated titanium chips, was used to create the protective atmosphere. Typical oxygen impurity levels in the inert gas, monitored continuously throughout the heat treatment, were below  $10^{-7}$  ppm by weight (one part impurity in  $10^{13}$  parts inert gas). Temperature was monitored by a thermocouple located near the samples within the hot zone.

#### 3.2 Mechanical Test Specimen Preparation

Specimens prepared for mechanical testing were fabricated utilizing a powder metallurgy process. The preparation of most intermetallic compounds is difficult and is attributed to either volatilization during melting, cracking during cool-down after solidification, reaction with apparatus components during hot pressing or HIPing, or oxidation during heat treatments. These difficulties were considered before arriving at a suitable technique for sample fabrication.

The procedure selected for specimen preparation consists of (1) arc-melting of materials to the desired composition (2) crushing, attriting and screening to fine powders ( $-325$  mesh or  $\leq 44\mu$ ) (3) consolidation by vacuum hot pressing and (4) EDM machining and mechanically polishing the surfaces to a 600 grit ( $\leq 27\mu$ ) surface finish. Comminution of the arc-melted buttons was accomplished using a standard ball mill with tungsten carbide balls under an inert (argon) environment.

This fabrication approach was used to achieve the cleanest possible material (low interstitials and contaminants) with the best possible homogeneity. High sample densities are required during the consolidation step to ensure representative mechanical properties. To accomplish

this, all of the compositions were prepared by vacuum hot pressing at 1500-1650°C/70-105 MPa/1-2 hours. 3.2 cm X 5.7 cm graphite dies with molybdenum foil liners and an alumina release agent were used for the vacuum hot pressing.

### 3.3 Characterization

Optical Microscopy (OM), electron probe microanalysis (EPMA), X-Ray Diffraction (XRD), and wet-chemistry by inductively coupled plasma/atomic emission spectroscopy (ICP) were used to characterize the structure and composition of MoSi<sub>2</sub> compositions.

The microstructure of MoSi<sub>2</sub> with the C11b crystal structure was determined by optical means under polarized light. Grain structures are clearly evident in this imaging mode. MoSi<sub>2</sub> samples with the C40 crystal structure were chemically etched with Murakami's Reagent (10g K<sub>3</sub>Fe[CN]<sub>6</sub> + 10g KOH or NaOH + 100 ml H<sub>2</sub>O) to reveal grain structure.

Microstructural phase analysis of various MoSi<sub>2</sub> compositions were determined by a Cameca MBX scanning electron microprobe (EPMA) equipped with three wavelength spectrometers and a Kevex Sigma energy dispersive spectrometer. Phase contrast was provided by backscattered electron imaging. Compositions were determined by wavelength dispersive spectroscopy (WDS) using pure elemental standards and ZAF corrections.

Crystal structures were determined by x-ray diffraction (XRD) using a Rigaku rotating anode x-ray system and complementary JCPDS data bank for crystallographic identification. XRD with 2θ scans from 20 to 80° were used.

### 3.4 Mechanical Testing

Specimens prepared for four-point flexure testing exhibited dimensions of approximately 4 mm (width) x 1 mm (thickness) x 30 mm (length). Testing was performed under argon in an all metal tungsten-element vacuum furnace. The molybdenum fixture contains alumina contact rods with a geometry of major span = 25.4 mm; minor span = 12.7 mm. Displacement was measured using a center point contact extensometer. Measurements of stress, modulus, and ductility were determined from outputted load-displacement curves.

Specimens for three-point K<sub>IC</sub> flexure testing had the same dimensions as the four-point flexure specimens with the addition of a notch which was mechanically cut into the sample using a low speed diamond saw. The notch depth was one-half of the specimen thickness.

Compression samples for the determination of strength and minimum creep rates had dimensions of approximately 4 mm x 4 mm x 10 mm (height). Testing was performed in the equipment described for flexural testing except that SiC compression surfaces were used. Creep rates were determined from time-displacement plots with test durations of 1000 seconds at each discrete increment of stress. One sample for each temperature was used to measure the minimum creep rate at several stress levels.

## 4. RESULTS AND DISCUSSION

### 4.1 Phase I Alloy Screening

Six elemental modifications were selected for evaluation. Aluminum, boron and germanium substitutions for silicon and hafnium, niobium and rhenium substitutions for molybdenum were selected for alloy screening. These modifications will serve to evaluate the effects of crystal structure, substitutional alloying, atomic radii, and e/a ratio as well as clarification or confirmation of phase boundaries. The initial samples for evaluation contained substitutions of 50 percent (16.7 atomic percent when substituted for molybdenum and 33.3 atomic percent when substituted for silicon) and were prepared by arc-melting and homogenization heat treatment at 1400°C for 48 hours. Additional samples of other compositions to better define phase boundaries were also prepared by arc-melting. Phase analyses were performed by x-ray diffraction (XRD) and electron probe microanalysis (EPMA). The results are discussed below.

#### 4.1.1 Aluminum Modifications

The composition of  $\text{Mo}(\text{Si}_{0.5}\text{Al}_{0.5})_2$  exhibited the C40 hexagonal crystal structure and the lattice parameter is consistent with that found by Nowotny in x-ray card 10-277. The XRD results are summarized in Table 3. Additional compositions containing 5 and 40.5 atomic percent aluminum,  $\text{Mo}(\text{Si}_{0.92}\text{Al}_{0.08})_2$  and  $\text{Mo}(\text{Si}_{0.39}\text{Al}_{0.61})_2$  respectively, were also prepared to better define solubilities and phase boundaries. EPMA results generally confirm the phase diagram and solubility limits observed by previous investigators<sup>21</sup>. Backscatter electron images (BSE) along with the EPMA phase analyses are shown in Figs. 6, 7 and 8. The phase boundaries bounded by the C40 phase were found to occur at aluminum concentrations of 8.6 and 41.6 atomic percent, compositions of  $\text{Mo}(\text{Si}_{0.87}\text{Al}_{0.13})_2$  and  $\text{Mo}(\text{Si}_{0.38}\text{Al}_{0.62})_2$  respectively, at 1400°C. The solubility of aluminum in  $\text{MoSi}_2$  is 3.1 atomic percent. Based on these results, two compositions (20 and 50% aluminum substitutions for silicon) of  $\text{Mo}(\text{Si}_{0.8}\text{Al}_{0.2})_2$  and  $\text{Mo}(\text{Si}_{0.5}\text{Al}_{0.5})_2$  were selected for evaluation of properties. Both of these compositions have the C40 crystal structure.

#### 4.1.2 Boron Modifications

The composition containing 50 percent substitution of boron for silicon [33.3 atomic percent B or  $\text{Mo}(\text{Si}_{0.5}\text{B}_{0.5})_2$ ] exhibited a multiphase structure consisting of  $\text{MoSi}_2$  (with the C11<sub>b</sub> structure) and borides approximating the compositions  $\text{MoB}$  and  $\text{MoB}_2$ . A BSE image along with the EPMA phase analysis is shown in Fig. 9. These results confirm previous studies<sup>22</sup> and indicate no appreciable solubility of B in  $\text{MoSi}_2$  and Si in " $\text{MoB}_2$ ". Based on these results, boron modifications were not selected for further evaluation.

#### 4.1.3 Germanium Modifications

The compositions containing 10, 25, and 50 percent germanium substitutions for silicon [6.7, 16.7, and 33.3 atomic percent Ge or respective compositions of  $\text{Mo}(\text{Si}_{0.9}\text{Ge}_{0.1})_2$ ,  $\text{Mo}(\text{Si}_{0.75}\text{Ge}_{0.25})_2$ , and  $\text{Mo}(\text{Si}_{0.5}\text{Ge}_{0.5})_2$ ] exhibited the single phase  $\text{C11}_b$  crystal structure indicating complete solubility of germanium in  $\text{MoSi}_2$  in the region of interest. A BSE image along with the EPMA phase analysis is shown in Fig. 10. As shown by the results in Table 3, the lattice parameters generally followed the rule of mixtures and increased with increasing germanium concentrations. These modifications have been selected for properties evaluation.

#### 4.1.4 Hafnium Modifications

The composition containing 50 percent hafnium substitution for molybdenum [16.7 atomic percent Hf or  $(\text{Mo}_{0.5}\text{Hf}_{0.5})\text{Si}_2$ ] in  $\text{MoSi}_2$  exhibited a two phase structure of  $\text{MoSi}_2$  (with the  $\text{C11}_b$  structure) and  $\text{HfSi}_2$  (with the C49 structure). This result verifies phase diagram results by other investigators<sup>23</sup> and indicates very low solubilities of Hf in  $\text{MoSi}_2$  and Mo in  $\text{HfSi}_2$ . A BSE image along with the EPMA phase analysis is shown in Fig. 11. Based on these results, hafnium modifications were not selected for further evaluation.

#### 4.1.5 Niobium Modifications

The composition containing a 50 percent niobium substitution for molybdenum [16.7 atomic percent Nb or  $(\text{Mo}_{0.5}\text{Nb}_{0.5})\text{Si}_2$ ] exhibited the C40 hexagonal crystal structure. An additional composition containing 6.3 atomic percent Nb [ $(\text{Mo}_{0.81}\text{Nb}_{0.19})\text{Si}_2$ ] was prepared to better define the solubility limits. The results of EPMA analyses indicate solubility limits that are different than that observed by other investigators<sup>24</sup>. BSE images along with the EPMA phase analyses are shown in Figs. 12 and 13. The solubility of niobium in  $\text{MoSi}_2$  ( $\text{C11}_b$  structure) is 1.5 atomic percent,  $(\text{Mo}_{0.95}\text{Nb}_{0.05})\text{Si}_2$ , while the solubility of molybdenum in  $\text{NbSi}_2$  (C40 structure) is 26.5 atomic percent,  $(\text{Mo}_{0.8}\text{Nb}_{0.2})\text{Si}_2$ , at 1400°C. XRD results in Table 3 indicate the lattice parameter of  $\text{MoSi}_2$  (C40 structure) increases linearly with increasing niobium concentrations. Based on these results, compositions with 9.7 and 16.7 atomic percent niobium substitutions for molybdenum,  $(\text{Mo}_{0.79}\text{Nb}_{0.29})\text{Si}_2$  and  $(\text{Mo}_{0.5}\text{Nb}_{0.5})\text{Si}_2$ , in  $\text{MoSi}_2$  were selected for further evaluation. Both of these alloys lie within the C40 phase field.

#### 4.1.6 Rhenium Modifications

The compositions containing 10, 25, and 50 percent rhenium substitutions for molybdenum [3.3, 8.3, and 16.7 atomic percent Re or  $(\text{Mo}_{0.9}\text{Re}_{0.1})\text{Si}_2$ ,  $(\text{Mo}_{0.75}\text{Re}_{0.25})\text{Si}_2$ , and  $(\text{Mo}_{0.5}\text{Re}_{0.5})\text{Si}_2$  respectively] exhibited the  $\text{C11}_b$  tetragonal structure. A typical BSE image along with the EPMA phase analysis is shown in Fig. 14. The results indicate complete solubility in the  $\text{ReSi}_2$ - $\text{MoSi}_2$  system. XRD results in Table 3 indicate the lattice parameter decreases linearly with increasing rhenium concentrations. These compositions were selected for further evaluation.

## 4.2 Phase I Property Evaluation

### 4.2.1 Mechanical Properties

The mechanical properties have been determined by four point flexural testing. The testing was performed at room temperature and at elevated temperatures to determine strength, ductility, and ductile-to-brittle transition temperature (DBTT). These results are summarized in Table 4. In general, no ductility was observed below the DBTT. The strength of the alloys appear to increase with increasing temperatures while the elastic modulus decreases with increasing temperature. The DBTT was not altered significantly with the alloy compositions and crystal structures evaluated. The observed DBTT appears to be higher than that reported in the literature<sup>4</sup> and may be attributed to the processing techniques used. These samples exhibit high purities and low interstitial contents which may explain the observed higher DBTTs.

### 4.2.2 Oxidation Resistance

Samples for the evaluation of oxidation resistance and mechanical properties were prepared in the same manner. A procedure of arc-melting/powder comminution/VHP consolidation was utilized. Oxidation testing was performed at 1400°C for 22 hours and 124 hours under isothermal conditions. This test was a screening test to determine if the alloy modifications selected would degrade oxidation resistance.

The weight change results shown in Table 5 indicate none of the alloy modifications significantly decreased the oxidation resistance of MoSi<sub>2</sub>. However, the samples containing 50% aluminum substitutions exhibited spalling (apparently due to the formation of a mixed oxide scale) while the composition containing 50% substitution of rhenium for molybdenum exhibited large initial weight losses.

## 4.3 Phase II Alloy Screening

Six alloying elements were evaluated in the Phase I effort. The ternary alloy modifications of MoSi<sub>2</sub> include Al, B, Ge, Hf, Nb, and Re. Based on the results in Phase I which concluded that B and Hf have virtually no solubility in MoSi<sub>2</sub>, these modifications were not selected for further evaluation.

Four alloying elements were selected for the evaluation of mechanical properties: Aluminum and germanium substitutions for silicon in MoSi<sub>2</sub> and niobium and rhenium substitutions for molybdenum in MoSi<sub>2</sub>. All alloy compositions selected in this phase of the program are single phase. Alloy compositions for the last phase of this program were either near the C11b/C40 two phase boundaries or within the two phase field. These modifications were served to evaluate the effects of crystal structure, substitutional alloying, atomic radii size, and e/a ratio on mechanical properties. Samples of the selected compositions were prepared by arc-



melting, comminution, blending, and vacuum hot pressing. Samples prepared using this methodology have microstructures typified by the baseline  $\text{MoSi}_2$  microstructure shown in Fig. 15.

#### 4.3.1 Aluminum Modifications

The compositions of  $\text{Mo}(\text{Si}_{0.8}\text{Al}_{0.2})_2$  and  $\text{Mo}(\text{Si}_{0.5}\text{Al}_{0.5})_2$  exhibiting the C40 hexagonal crystal structure were selected for properties evaluation. These compositions both lie within the C40 phase boundaries defined previously at  $\text{Mo}(\text{Si}_{0.87}\text{Al}_{0.13})_2$  and  $\text{MoAl}_2$ .

#### 4.3.2 Germanium Modifications

The compositions  $\text{Mo}(\text{Si}_{0.9}\text{Ge}_{0.1})_2$  and  $\text{Mo}(\text{Si}_{0.75}\text{Ge}_{0.25})_2$  exhibiting a single phase C11<sub>b</sub> crystal structure with complete solubility of germanium in  $\text{MoSi}_2$  were selected for properties evaluation.

#### 4.3.3 Niobium Modifications

The compositions  $(\text{Mo}_{0.71}\text{Nb}_{0.29})\text{Si}_2$  and  $(\text{Mo}_{0.5}\text{Nb}_{0.5})\text{Si}_2$  exhibiting the C40 hexagonal crystal structure were selected for properties evaluation. These compositions both lie within the C40 phase boundaries defined previously at  $(\text{Mo}_{0.8}\text{Nb}_{0.2})\text{Si}_2$  and  $\text{NbSi}_2$ .

#### 4.3.4 Rhenium Modifications

The compositions  $(\text{Mo}_{0.9}\text{Re}_{0.1})\text{Si}_2$ ,  $(\text{Mo}_{0.75}\text{Re}_{0.25})\text{Si}_2$ ,  $(\text{Mo}_{0.5}\text{Re}_{0.5})\text{Si}_2$  exhibiting the C11<sub>b</sub> tetragonal structure with complete solubility of rhenium in  $\text{MoSi}_2$  were selected for properties evaluation.

### 4.4 Phase II Properties Evaluation

#### 4.4.1 Mechanical Properties

##### 4.4.1.1 Four-Point Flexural Testing

The mechanical properties for the baseline  $\text{MoSi}_2$  and modifications with Al, Ge, Nb, and Re have been determined by four point flexural testing. The testing was performed at room temperature and at elevated temperatures to determine strength, ductility, and ductile-to-brittle transition temperature (DBTT). These results are summarized in Table 6. In general, no ductility was observed below the DBTT. The strength of the alloys appear to increase with increasing temperatures while the elastic modulus decreases with increasing temperature. The DBTT was not altered significantly with the alloy compositions and crystal structures evaluated. The observed DBTT were all in the range 1250 to 1350°C.

The results in Table 6 also indicate that strengthening was significant with the niobium alloy modification at elevated temperatures.

#### 4.4.1.2 Three-Point Flexural $K_{IC}$ Testing

The fracture toughness was determined using a notched specimen tested in three point flexure. The results for the baseline  $MoSi_2$  and the Al, Ge, Nb, and Re modified alloys are shown in Table 7. Generally, all of the alloys have low fracture toughnesses below the DBTT (1-4 MPa  $\sqrt{m}$ ) and improved fracture toughnesses when tested above the DBTT.

The niobium modified alloy exhibited a higher fracture toughness at elevated temperatures than either the baseline  $MoSi_2$  or the aluminum, germanium, or rhenium modified alloys. This is most likely attributed to its higher elevated temperature strength.

#### 4.4.1.3 Compression Testing

Compression testing was performed to determine suitable stresses to perform compressive creep testing. A sample of each composition was used to determine the 0.1% offset yield stress throughout the temperature range 1000-1400°C. The first test was performed at 1400°C to a strain of 0.1%. Subsequent tests were performed on the same sample to a similar strain level with decrements of 100°C.

These results are shown in Table 8 and Fig. 16 and indicate that the addition of niobium dramatically improves the strength of  $MoSi_2$  throughout the temperature range. Significant strengthening is also observed with aluminum modifications at the lower temperatures. Germanium modifications were found to reduce the strength of  $MoSi_2$ . Rhenium modifications appear to increase the strength of  $MoSi_2$  based on the limited data generated. Difficulties encountered during testing limited the amount of fully reduced data for the rhenium modified alloys.

#### 4.4.1.4 Compressive Creep Testing

Compressive creep testing was performed for the baseline  $MoSi_2$  and the Al, Ge, Nb, and Re modifications to determine the minimum creep rate at temperatures of 1000, 1200, and 1400°C. One test specimen was used at each temperature and creep rates were determined starting at the lowest test stresses. Loading was maintained at each stress level for 1000 seconds to determine minimum creep rates. An approximation of the creep ductility was determined by totaling the creep strains for all of the applied stress levels at one test temperature.

The minimum creep rates for each composition are listed in Tables 9, 10, and 11 and shown in Figs. 17, 18, and 19 for test temperatures of 1000, 1200, and 1400°C respectively. The total creep strain at each test temperature is tabulated in Table 12. These results indicate that

modifications with germanium generally decrease creep resistance. The addition of aluminum improved creep strength only at the lower temperatures. The addition of rhenium improved creep resistance by about an order of magnitude and is consistent with prior work<sup>6</sup>. However, this improvement in creep resistance is accompanied by a significant reduction in the creep ductility of the alloy. The addition of niobium to MoSi<sub>2</sub> also provided a significant improvement in the creep resistance by about an order of magnitude throughout the temperature range of interest while not debiting the creep ductility of the alloy. The need to improve the high temperature strength of MoSi<sub>2</sub> appears to have been met with the additions of Re and Nb. The addition of Nb offers the best promise since compressive strength and creep strength were increased significantly without a debit in alloy ductility.

The stress exponent was calculated from the data in Figs. 17, 18, and 19. Generally,  $n=3-5$  at 1000°C,  $n=3$  at 1200°C, and  $n=2$  at 1400°C. These  $n$  values are in the "power law creep" region where vacancy diffusion assisted dislocation climb occurs.

#### 4.5 Phase III Alloy Screening

Six alloying elements were in Phase I of this program. The ternary alloy modifications of MoSi<sub>2</sub> include Al, B, Ge, Hf, Nb, and Re. Based on this work, Al, Ge, Nb and Re modifications were selected for further evaluation of properties.

Four alloying elements were selected for evaluation of mechanical properties in the Phase II effort: Aluminum and germanium substitutions for silicon in MoSi<sub>2</sub> and niobium and rhenium substitutions for molybdenum in MoSi<sub>2</sub> were selected. All alloy compositions selected in this phase of the program were single phase. The mechanical properties testing during the second year effort indicated improvements in creep strength imparted by additions of either niobium or rhenium<sup>22</sup>.

Alloy compositions for this phase of the program are niobium and/or rhenium modifications near the C11<sub>b</sub>/C40 two phase boundaries or within the two phase field. These modifications serve to evaluate the effects of crystal structure, substitutional alloying, atomic radii size, and  $e/a$  ratio on mechanical properties. Samples of the selected compositions were prepared by the standard arc-melting, comminution, blending, and vacuum hot pressing used in Phases I and II.

##### 4.5.1 Niobium Modifications

The compositions (Mo<sub>0.97</sub> Nb<sub>0.03</sub>)Si<sub>2</sub> with the C11<sub>b</sub> tetragonal crystal structure; (Mo<sub>0.93</sub> Nb<sub>0.07</sub>)Si<sub>2</sub> and (Mo<sub>0.85</sub> Nb<sub>0.15</sub>)Si<sub>2</sub> with the two phase C40 + C11<sub>b</sub> structure; and (Mo<sub>0.71</sub> Nb<sub>0.29</sub>)Si<sub>2</sub> exhibiting the C40 hexagonal crystal structure were selected for properties evaluation.

#### 4.5.2 Rhenium Modifications

The composition  $(\text{Mo}_{0.9}\text{Re}_{0.1})\text{Si}_2$  exhibiting the  $\text{C11b}$  tetragonal structure with complete solubility of rhenium in  $\text{MoSi}_2$  was selected for properties evaluation. The mechanical properties measured during the second year indicated the low rhenium modification exhibited the best combination of mechanical properties and oxidation resistance.

#### 4.5.3 Niobium and Rhenium

An alloy incorporating both niobium and rhenium was prepared with the composition  $(\text{Mo}_{0.61}\text{Nb}_{0.29}\text{Re}_{0.10})\text{Si}_2$ . This single phase composition was selected based on the excellent properties achieved with the niobium and rhenium alloy modifications.

### 4.6 Phase III Properties Evaluation

#### 4.6.1 Mechanical Properties

##### 4.6.1.1 Four-Point Flexural Testing

The mechanical properties for the Nb, Re and Nb + Re modifications have been determined by four point flexural testing. The testing was performed at room temperature and at elevated temperatures to determine strength, ductility, and ductile-to-brittle transition temperature (DBTT). These results are summarized in Table 13. In general, no ductility was observed below the DBTT. The strength of the alloys appear to increase with increasing temperatures while the elastic modulus decreases with increasing temperature. The DBTT was not altered significantly with the alloy compositions and crystal structures evaluated. The observed DBTT appears to be higher than that reported in the literature<sup>4</sup> and may be attributed to the processing techniques used. Higher purities with lower interstitial containing samples were evaluated under this program.

The results in Table 13 also indicate that strengthening was significant with the niobium alloy modification at elevated temperatures.

##### 4.6.1.2 Three-Point Flexural $K_{IC}$ Testing

The fracture toughness was determined using a notched specimen tested in three point flexure. The results for the Nb, Re and Nb + Re modified  $\text{MoSi}_2$  are shown in Table 14. Generally, all of the alloys have low fracture toughnesses ( $1-4 \text{ MPa}\cdot\sqrt{\text{m}}$ ) below the DBTT and improved fracture toughnesses when tested above the DBTT.

The niobium and/or rhenium modified alloys containing 9.5 atomic percent Nb exhibited a slightly higher fracture toughness at elevated temperatures than either the other modified alloys.

#### 4.6.1.3 Compression Testing

Compression testing was performed to determine suitable stresses to perform compressive creep testing. A sample of each composition was used to determine the 0.1% offset yield stress throughout the temperature range 1000-1400°C. The first test was performed at 1400°C to a strain of 0.1%. Subsequent tests were performed on the same sample to a similar strain level with decrements of 100°C.

The results are shown in Table 15 and Fig. 20 and indicate the addition of niobium, rhenium, and niobium + rhenium improves the strength of MoSi<sub>2</sub> throughout the temperature range.

#### 4.6.1.4 Compressive Creep Testing

Compressive creep testing was performed for the Nb, Re, and Nb + Re modifications to determine the minimum creep rate at temperatures of 1000, 1200, and 1400°C. One test specimen was used at each temperature and creep rates were determined starting at the lowest test stresses. Loading was maintained at each stress level for 1000 seconds to determine minimum creep rates. An approximation of the creep ductility was determined by totaling the creep strains for all of the applied stress levels at one test temperature.

The minimum creep rates for each composition are listed in Tables 16, 17, and 18 and shown in Figs. 21, 22, and 23 for test temperatures of 1000, 1200, and 1400°C respectively. The total creep strain at each test temperature is tabulated in Table 19. The addition of rhenium, niobium, and Nb + Re improved creep resistance by an order of. However, this improvement in creep resistance is accompanied by a significant reduction in the creep ductility of the Re modified alloy. The addition of niobium and Nb + Re to MoSi<sub>2</sub> provided a significant improvement in the creep resistance while not debiting the creep ductility of the alloy.

The stress exponent was calculated from the data in Figs. 21, 22, and 23. Generally,  $n=3-7$  at 1000°C,  $n=3$  at 1200°C, and  $n=2$  at 1400°C. These  $n$  values are in the "power law creep" region where vacancy diffusion assisted dislocation climb occurs except at 1000°C. The stress exponent  $n = 5-7$  for several alloys when tested at the highest stress levels (about 1000 Mpa) at 1000°C suggests a mechanism where thermally activated dislocation glide is the rate-controlling step, perhaps associated with a significant back stress or threshold stress.

#### 4.6.2 Oxidation Testing

Samples for evaluation of oxidation resistance were prepared in the same manner as the samples used for mechanical properties evaluation. Samples were polished to a 600 grit finish prior to oxidation testing. They were tested in air at 1400°C for 20 hours and 120 hours under isothermal conditions. This test was to determine if the alloy modifications selected would degrade oxidation resistance.

The weight change results shown in Table 20 indicate all of the alloy modifications did not debit the excellent oxidation resistance of  $\text{MoSi}_2$ . The  $\text{MoSi}_2$  weight change results are included from the first oxidation test for comparison purposes.

#### 4.7 Atomic Modeling

A series of atomic modeling calculations was done for  $\text{MoSi}_2$  to determine the feasibility of using efficient simulation tools to assist in the interpretation of properties, specifically bonding and the influence of alloying. This work was mostly carried out with internal funds, and was facilitated by Mark Eberhart of the Colorado School of Mines.

The LKKR<sup>27</sup> code had been installed at UTRC and was successfully used to model antiphase boundaries in  $\text{Ni}_3\text{Al}$ . The baseline  $\text{C11}_b$  structure is shown in Figure 24. An input file was created for  $\text{MoSi}_2$  and the potentials were converged on an Alliant minisupercomputer. The charge density was then computed. These calculations took about one day. For visualization purposes, the charge density was converted from a 2D to a 3D structure in the "PLOT3D" format for mesh co-ordinates and relevant quantities. To avoid heavy contouring near the nucleus, another routine was used to crop the data; this allows one to focus on the bonding electrons. It was found that the gradient of charge density was useful for locating bonds within a structure. A routine was written and used to compute the x, y and z components of the charge density.

The UTRC visualizers "VISA" and "VISA-GOLD" were used to examine the charge density. A related commercial visualizer, "FIELDVIEW" was also used. An example of a set of charge density contours on the (001) plane is shown in Figure 25. It can be seen that the expected four-fold symmetry is not completely satisfied. However, some indication of elongation of the charge density around Si atoms towards the central Mo atom can be seen for the (200) section in Figure 26. Three dimensional viewing of the charge density using "isosurfaces" showed sharp spikes in the region where bonds were expected. It was concluded that these were associated with numerical noise and that the LKKR code was not adequate to carry out precise calculations at the low charge densities in the interatomic regions.

The LASTO code was subsequently installed at UTRC to run on an IBM RISC 6000 workstation using the "Distributed Queuing System" tool for distributed computing on a network of about a dozen such workstations. The most available workstation was selected and a single processor was used. Scripts were built to compile, time and track the submitted jobs. Machines with 128MB of RAM were used. Data were stored on a DECstation running Ultrix, or on an Epoch archival file server. A "Builder" was installed to facilitate the building of molecular models. Symmetry files and the related input files for structure and initial potentials were built and tested for Al and Ag (fcc);  $\text{NiAl}$  and  $\text{CoAl}$  ( $\text{B}_2$ );  $\text{Ni}_3\text{Al}$  ( $\text{L1}_2$ );  $\text{Ti}_3\text{Al}$  ( $\text{L1}_0$ ); Fe (bcc); Co (hcp); and  $\text{MoSi}_2$  ( $\text{C11}_b$ ).

Again, the potentials were converged and then charge density distributions were computed at various resolutions. Tools were used to convert to PLOT3D, crop and compute gradients. These calculations took about one day of CPU time. The FIELDVIEW isosurface and "cutting plane" tools were used to carry out viewing. A SGI indigo2 extreme workstation was used to view the charge density. The "snapshot" and "showcase" tools were used to create, size and convert images into the Adobe PostScript format for printing as black & white or color figures. A "surface" (filled) view of the charge density on the (110) plane is shown in Figure 27. The Mo nuclei can clearly be seen at the center and the corners in this plot. The other six atom centers are Si.

These results were generally much better behaved (smoother) than the LKKR calculations. As a result, contour plots, such as seen in Figures 28 and 29 show elongation of the Si electrons toward the Mo. The symmetry is very close to what is expected. Bonds can be clearly seen in Figure 28. They are in the expected directions. Assessment of the strength of the bonds is subject to interpretation at this point, but it can be said that this material has a strong covalent component since the electrons are concentrated along the bond lines. This would not be the case for a metal, such as Ni or even an intermetallic that behaves like a metal, e.g.  $\text{Ni}_3\text{Al}$ . A full cell view of the charge density at a value where the contours overlap significantly is shown in Figure 30. The distortion of the charge around the silicon atoms toward the molybdenum sites is clearly evident.

Such figures can be used to rationalize cleavage behavior, but guidance for alloy design is not immediately obvious. Attempts to add third elements to such a calculation for the case of  $\text{Ni}_3\text{Al}$  are now underway; however, this is challenging on a single processor workstation, at least for anything other than a major addition. A more efficient version of LASTO is about to be released by James McLaren of Tulane University. This upgraded software and continual advances in hardware capability should assist in carrying out such challenging calculations. Similar tools are routinely used in the petrochemical, pharmaceutical and semiconductor industries, and it is only a matter of time before they are used by the Materials Community as well.

## 5. CONCLUSIONS

1. Six elemental modifications of  $\text{MoSi}_2$  have been evaluated. They are Al, B, and Ge substitutions for Si and Hf, Nb, and Re substitutions for Mo.
2. B and Hf modifications exhibited two phase or multiphase structures with very little solubility in  $\text{MoSi}_2$ .
3. Al and Nb substitutions for Si and Mo, respectively, in  $\text{MoSi}_2$  resulted in alloys with the C40 hexagonal crystal structure.
4. Ge and Re substitutions for Si and Mo, respectively, in  $\text{MoSi}_2$  resulted in alloys with the  $\text{C11}_b$  tetragonal crystal structure.
5. Most of the analyses confirm the validity of available phase diagrams although the results presented here indicate a need to refine the solubility limits.
6. Isothermal oxidation testing indicates no significant debit in oxidation resistance at  $1400^\circ\text{C}$  due to ternary alloying. Alloys containing higher concentrations of ternary elements may exhibit reduced oxidation resistances.
7. Mechanical properties as determined by four-point flexural testing indicate DBTTs were in the temperature range  $1250\text{-}1350^\circ\text{C}$  for all of the modifications evaluated.
8. The fracture toughness of the baseline and all of the modified alloys were  $1\text{-}4\text{ MPa}\cdot\sqrt{\text{m}}$  below the DBTT and slightly higher ( $1\text{-}13\text{ MPa}\cdot\sqrt{\text{m}}$ ) above the DBTT. The 9.5 atomic percent niobium alloys with the C40 structure exhibited a better fracture toughness ( $5\text{-}13\text{ MPa}\cdot\sqrt{\text{m}}$ ) at elevated temperatures.
9. The compressive strength of  $\text{MoSi}_2$  was improved significantly with the addition of Al, Nb and Re. Ge did not improve the mechanical properties of  $\text{MoSi}_2$ , while Re improved the elevated temperature strength. The strength increase due to Al was not retained at the highest test temperature ( $1400^\circ\text{C}$ ). Nb and Re additions increased strength at all temperatures tested..
10. The compressive minimum creep rate was improved with the additions of Nb and Re. The dramatic reduction in the minimum creep rate of the Re modified alloys was accompanied by a reduction in the creep ductility. Nb modified alloys also exhibited a significant reduction in the compressive minimum creep rate and a reduction in creep ductility was not observed when compared to the baseline  $\text{MoSi}_2$ .



11. The LASTO code is more effective in terms of computing interatomic charge density than the LKKR code. Such charge density calculations give insight as to the bond strength and anisotropy in  $\text{MoSi}_2$ .

## 6. REFERENCES

1. D. L. Anton, D. B. Snow, L. H. Favrow, and A. F. Giamei, "Dispersion Strengthening of High Temperature Niobium Alloys", Final Report R89-917437-3 on AFOSR Contract F49620-86-C-0053, 7/1989.
2. E. Fitzner, Plansee Proc. 2nd Seminar, Reutte/Tyrol, 1955, Pergamon Press, London, 1956.
3. G. H. Meier, D. Berztiss, and F. S. Pettit, "Oxidation of  $\text{MoSi}_2$  in the Temperature Range 500-1200°C", presented at Aeromat '91, May 23, 1991.
4. P.J. Meschter and D. S. Schwartz, "Silicide-Matrix Materials for High Temperature Applications", *Journal of Metals*, V.41 N11, pp.52-55, 11/89.
5. E. Fitzner and J. Schlichting, Planseeber. Pulvermetall., 20 (2), pp. 110-128, 1972.
6. D. L. Anton and D. M. Shah, "Development Potential of Advanced Intermetallic Materials", Final Report WRDC-TR-90-4122, WRDC Contract F33615-87-C-5214, 2/91.
7. J. J. Petrovic and R. E. Honnel, "MoSi<sub>2</sub>-Based Composites", ONR Contract and Presented at DARPA/DoD Review at P&W-West Palm Beach, FL, 2/90.
8. V. C. Nardone and J. R. Strife, "Development of Microstructurally Toughened Composites", Annual report R90-917705-3, ONR Contract N00014-87-C-0406, 8/90.
9. N. V. Ageev, Phase Diagrams of Metallic Systems, NASA Technical Translation, NASA TT F-17296, 1959-1976.
10. P. S. Frankwicz and J. H. Perepesko, "Phase Stability and Solidification Pathways in MoSi<sub>2</sub> Based Alloys", *Mat. Res. Soc. Symp. Proc. Vol. 213*, Materials Research Society, 1991.
11. B. Massalski, Binary Alloy Phase Diagrams, ASM, 1986.
12. P. L. Martin, Rockwell Science Center, Private Communications.
13. L. Brewer, "Chemical Bonding Theory Applied To Metals", Alloying, J. L. Walter ed., ASM, 1988.
14. D. G. Pettifor, "Structure Maps For Pseudobinary and Ternary Phase", *Materials Science and Technology*, Vol. 4, pp. 675-691, 8/1988

15. Y. Umakoshi, presented at the TMS Fall Meeting, 1989.
16. A. E. Dwight and P. A. Beck, "Closed-Packed Ordered Structures in Binary AB<sub>3</sub> Alloys of Transition Elements" Trans. AIME, V. 215, pp. 976-979, 1959.
17. M. V. Nevitt, "Electronic Structure of Alloy Chemistry of the Transition Elements", Alloy Chemistry of Transition Elements, Editor: P.A. Beck, Interscience, J. Wiley and Sons, p. 101, 1962.
18. C. T. Liu, "Physical Metallurgy and Mechanical Properties of Ductile Ordered Alloys (Fe,Co,Ni)<sub>3</sub>V", Int. Met. Rev., V. 29, pp. 168-194, 1984.
19. F. Laves, Intermetallic Compounds, Editor: J. H. Westbrook, J. Wiley and Sons, New York, NY, 1967.
20. P. A. Beck, "Closed-Packed Ordered Alloys", Advances in X-Ray Analysis, V. 12, Editor: C. S. Barrett, Plenum, New York, pp. 1-21, 1969.
21. Ageer, N. V., Diagram Sostoyaniy Metallicheshikh Sistem, "VINITI" Press, Moscow, 1960 p. 100 and 1966, p 143
22. Ageer, N. V., Diagram Sostoyaniy Metallicheshikh Sistem, "VINITI" Press, Moscow, 1957
23. Ageer, N. V., Diagram Sostoyaniy Metallicheshikh Sistem, "VINITI" Press, Moscow, 1971, p. 270
24. Ageer, N. V., Diagram Sostoyaniy Metallicheshikh Sistem, "VINITI" Press, Moscow, 1965, p 234
25. S. Chin, D. L. Anton, and A. F. Giamei, "Advanced MoSi<sub>2</sub> Compositions", Annual report R93-970281-1 on AFOSR Contract F49620-92-C-0043, 9/93
26. S. Chin, D. L. Anton, and A. F. Giamei, "Advanced MoSi<sub>2</sub> Compositions", Annual report R93-970281-2 on AFOSR Contract F49620-92-C-0043, 10/94
27. J. M. MacLaren, S. Crampin, D. D. Vvedensky, R. C. Albers, and J. B. Pendry, "A layer Korringa-Kohn-Rostoker Electronic Structure Code for Bulk and Interface properties", Computer Physics Communications, 60, 365 (1990)

**TABLE 1 ATOMIC RADII**

<b>Element</b>	<b>Goldschmidt Radius (nm)</b>
<b>Si</b>	0.117
<b>B</b>	0.097
<b>C</b>	0.077
<b>Al</b>	0.143
<b>Ge</b>	0.139
<b>Mo</b>	0.140
<b>Ti</b>	0.147
<b>V</b>	0.136
<b>Cr</b>	0.128
<b>Zr</b>	0.160
<b>Nb</b>	0.147
<b>Hf</b>	0.159
<b>Ta</b>	0.147
<b>W</b>	0.141
<b>Re</b>	0.138

**TABLE 2 WET CHEMICAL ANALYSES**

Composition	Description	Weight Percent					
		Mo	Nb	Re	Si	Al	Ge
<b>MoSi<sub>2</sub></b>	Nominal	63.04			36.96		
	Actual	66.16			35.49		
<b>Mo(Si<sub>0.5</sub>Al<sub>0.5</sub>)<sub>2</sub></b>	Nominal	63.60			18.56	17.83	
	Actual	63.48			17.52	17.52	
<b>Mo(Si<sub>0.9</sub>Ge<sub>0.1</sub>)<sub>2</sub></b>	Nominal	59.53			31.40		9.06
	Actual	62.75			30.70		8.14
<b>Mo(Si<sub>0.75</sub>Ge<sub>0.25</sub>)<sub>2</sub></b>	Nominal	54.98			24.16		20.86
	Actual	57.17			23.97		18.62
<b>(Mo<sub>0.5</sub>Nb<sub>0.5</sub>)Si<sub>2</sub></b>	Nominal	31.89	30.88		37.23		
	Actual	31.85	29.15		34.87		
<b>(Mo<sub>0.9</sub>Re<sub>0.1</sub>)Si<sub>2</sub></b>	Nominal	53.64		11.45	34.91		
	Actual	56.48		11.10	33.38		
<b>(Mo<sub>0.75</sub>Re<sub>0.25</sub>)Si<sub>2</sub></b>	Nominal	41.23		26.57	32.20		
	Actual	43.19		25.90	30.76		
<b>(Mo<sub>0.5</sub>Re<sub>0.5</sub>)Si<sub>2</sub></b>	Nominal	24.34		47.24	28.42		
	Actual	24.94		46.77	26.81		

### TABLE 3 X-RAY DIFFRACTION - LATTICE PARAMETERS

[illegible]

TABLE 4 FOUR-POINT FLEXURE TEST RESULTS

Composition		Temp (°C)	UTS (MPa)	E (GPa)	$\epsilon$ (%)	DBTT (°C)
<b>Mo(Si<sub>0.5</sub>Al<sub>0.5</sub>)<sub>2</sub></b>		1200	207	117	0	~1250
		1300	139	123	>1.0	
<b>(Mo<sub>0.5</sub>Nb<sub>0.5</sub>)Si<sub>2</sub></b>		1300	346	169	0	~1350
		1400	244	147	>1.5	
<b>(Mo<sub>0.9</sub>Re<sub>0.1</sub>)Si<sub>2</sub></b>		RT	171	285	0	
		1000	232	331	0	
		1200	275	207	0	
		1300	261	229	0.1	~1350
		1400	241	104	>0.9	
<b>(Mo<sub>0.75</sub>Re<sub>0.25</sub>)Si<sub>2</sub></b>		RT	153	348	0	
		1000	234	372	0	
		1200	189	165	0	
		1300	171	179	0	
		1400	192	205	0.4	~1400
<b>(Mo<sub>0.5</sub>Re<sub>0.5</sub>)Si<sub>2</sub></b>		RT	200	371	0	
		1000	243	284	0	
		1200	231	235	0.1	~1250
		1300	191	138	>1.1	
		1400	170	137	>1.7	

**TABLE 5 ISOTHERMAL OXIDATION RESULTS (1400°C)**

Composition	Weight Change (mg/cm <sup>2</sup> )		Remarks
	22 hours	124 hours	
<b>MoSi<sub>2</sub></b>	+0.5	+1.2	
<b>Mo(Si<sub>0.5</sub>Al<sub>0.5</sub>)<sub>2</sub></b>	+1.5	+4.9	Scale spallation after 22h
<b>Mo(Si<sub>0.9</sub>Ge<sub>0.1</sub>)<sub>2</sub></b>	+1.7	+1.7	
<b>Mo(Si<sub>0.75</sub>Ge<sub>0.25</sub>)<sub>2</sub></b>	+1.0	+0.0	
<b>(Mo<sub>0.5</sub>Nb<sub>0.5</sub>)Si<sub>2</sub></b>	+1.5	+5.3	
<b>(Mo<sub>0.9</sub>Re<sub>0.1</sub>)Si<sub>2</sub></b>	+1.1	+4.3	
<b>(Mo<sub>0.75</sub>Re<sub>0.25</sub>)Si<sub>2</sub></b>	+1.3	+3.6	
<b>(Mo<sub>0.5</sub>Re<sub>0.5</sub>)Si<sub>2</sub></b>	- 6.6	- 5.6	



TABLE 6 FOUR-POINT FLEXURE TEST RESULTS

Composition	Temp (°C)	UTS (MPa)	E (GPa)	$\epsilon$ (%)	DBTT (°C)
MoSi <sub>2</sub>	RT	242	442	0	
	1200	326	273	0	~1250
	1300	299	217	>1.8	
Mo(Si <sub>0.8</sub> Al <sub>0.2</sub> ) <sub>2</sub>	RT	244	379	0	
	1200	305	247	0.1	~1250
	1300	193	154	>1.0	
Mo(Si <sub>0.5</sub> Al <sub>0.5</sub> ) <sub>2</sub>	1200	207	117	0	~1250
	1300	139	123	>1.0	
Mo(Si <sub>0.9</sub> Ge <sub>0.1</sub> ) <sub>2</sub>	RT	156	461	0	
	1200	248	192	0.1	~1250
	1300	160	183	>0.9	
	1400	111	145	>1.7	
Mo(Si <sub>0.75</sub> Ge <sub>0.25</sub> ) <sub>2</sub>	RT	96	292	0	
	1200	175	259	0	~1250
	1300	169	184	>1.6	
(Mo <sub>0.71</sub> Nb <sub>0.29</sub> )Si <sub>2</sub>	RT	175	383	0	
	1300	464	374	0.3	~1300
	1400	195	299	>1.8	
(Mo <sub>0.5</sub> Nb <sub>0.5</sub> )Si <sub>2</sub>	1300	346	169	0	~1350
	1400	244	147	>1.5	
(Mo <sub>0.9</sub> Re <sub>0.1</sub> )Si <sub>2</sub>	RT	171	285	0	
	1000	232	331	0	
	1200	275	207	0	
	1300	261	229	0.1	~1350
	1400	241	104	>0.9	
(Mo <sub>0.75</sub> Re <sub>0.25</sub> )Si <sub>2</sub>	RT	153	348	0	
	1000	234	372	0	
	1200	189	165	0	

		1300	171	179	0	~1350
		1400	192	205	0.4	
<b>(Mo<sub>0.5</sub>Re<sub>0.5</sub>)Si<sub>2</sub></b>		RT	200	371	0	
		1000	243	284	0	
		1200	231	235	0.1	~1250
		1300	191	138	>1.1	
		1400	170	137	>1.7	

**TABLE 7 THREE-POINT FLEXURE  $K_{IC}$  TEST RESULTS**

Composition		Temp (°C)		$K_{IC}$ (MPa·√m)
<b>MoSi<sub>2</sub></b>		RT		2.6
		1200		2.4
		1300		4.9
		1400		3.3
<b>Mo(Si<sub>0.8</sub>Al<sub>0.2</sub>)<sub>2</sub></b>		RT		3.0
		1300		4.5
		1400		3.1
<b>Mo(Si<sub>0.9</sub>Ge<sub>0.1</sub>)<sub>2</sub></b>		RT		1.2
		1300		6.4
		1400		2.2
<b>Mo(Si<sub>0.75</sub>Ge<sub>0.25</sub>)<sub>2</sub></b>		RT		2.5
		1200		3.2
		1300		4.9
		1400		2.2
<b>(Mo<sub>0.71</sub>Nb<sub>0.29</sub>)Si<sub>2</sub></b>		RT		3.5
		1300		13.0
		1400		6.3

**TABLE 8 COMPRESSIVE YIELD STRESS TEST RESULTS**

		0.1% Yield Stress (MPa)				
Composition		1000°C	1100°C	1200°C	1300°C	1400°C
MoSi <sub>2</sub>		799	661	455	365	165
Mo(Si <sub>0.8</sub> Al <sub>0.2</sub> ) <sub>2</sub>		1213	937	503	296	158
Mo(Si <sub>0.9</sub> Ge <sub>0.1</sub> ) <sub>2</sub>		710	579	303	179	117
Mo(Si <sub>0.75</sub> Ge <sub>0.25</sub> ) <sub>2</sub>		441	365	207	124	83
(Mo <sub>0.71</sub> Nb <sub>0.29</sub> )Si <sub>2</sub>		1158	834	737	489	351
(Mo <sub>0.9</sub> Re <sub>0.1</sub> )Si <sub>2</sub>		>1013		>331		>145
(Mo <sub>0.5</sub> Re <sub>0.5</sub> )Si <sub>2</sub>		>937		>372		186

**TABLE 9 MINIMUM CREEP RATES AT 1000°C**

Minimum Creep Rate (s <sup>-1</sup> )								
Stress (MPa)		MoSi <sub>2</sub>	13.3 Al	9.5 Nb	6.7 Ge	16.7 Ge	3.3 Re	16.7 Re
69						3.5E-7		
103						4.0E-7		
172						9.3E-7		
207							4.5E-8	
241			1.2E-7			3.0E-6		
276		7.0E-7			7.0E-7			
345		1.4E-6	2.5E-7	8.0E-8	1.0E-6			
414		1.9E-6			2.3E-6		1.4E-7	
483		3.0E-6	6.0E-7	2.0E-7	5.0E-6			1.2E-7
552		8.0E-6						
621		1.7E-5	1.0E-6	1.0E-6			3.2E-7	3.2E-7
758								5.3E-7
827			3.0E-6				8.5E-7	
896				3.9E-6			1.3E-6	7.5E-7
1034				1.0E-5				

**TABLE 10 MINIMUM CREEP RATES AT 1200°C**

Minimum Creep Rate (s <sup>-1</sup> )								
Stress (MPa)		MoSi <sub>2</sub>	13.3 Al	9.5 Nb	6.7 Ge	16.7 Ge	3.3 Re	16.7 Re
34			2.0E-7		7.0E-7	4.0E-7		
69		8.0E-7	6.0E-7		2.0E-6	2.5E-6	1.4E-7	
103		2.5E-6	8.0E-7	3.3E-7	4.0E-6	1.0E-5	2.0E-7	
138					1.5E-5		2.4E-7	
172		1.1E-5	2.1E-6				3.4E-7	1.2E-6
207				1.0E-6			4.1E-7	1.5E-6
241		4.0E-5	5.5E-6				6.8E-7	
276			8.5E-6				1.2E-6	2.6E-6
310				2.5E-6			2.5E-6	
345								7.0E-6
414				5.2E-6				
483				9.0E-6				

**TABLE 11 MINIMUM CREEP RATES AT 1400°C**

Minimum Creep Rate (s <sup>-1</sup> )								
Stress (MPa)		MoSi <sub>2</sub>	13.3 Al	9.5 Nb	6.7 Ge	16.7 Ge	3.3 Re	16.7 Re
14		2.0E-06	8.0E-07		1.7E-06	3.4E-07	1.0E-06	2.0E-06
28		5.0E-06	2.4E-06	4.0E-07	5.0E-06	2.8E-06	1.2E-06	6.0E-06
41			4.0E-06		1.1E-05	1.6E-05		1.1E-05
55		1.0E-05	8.0E-06	2.0E-06	2.5E-05			
69		2.0E-05		3.0E-06			2.7E-06	2.5E-05
83			1.2E-05				3.3E-06	
97			1.8E-05	5.0E-06			4.5E-06	
110		9.0E-05					6.5E-06	
124				8.0E-06				
152				1.1E-05				
179				1.4E-05				
207				1.9E-05				
221				2.0E-05				

TABLE 12 COMPRESSIVE CREEP DUCTILITY RESULTS

Composition	Creep Region of interest	Creep Ductility (%)		
		1000°C	1200°C	1400°C
MoSi <sub>2</sub>	I+II	2.0	4.7	18.9
	I+II+III	8.5	16.4	29.1
Mo(Si <sub>0.8</sub> Al <sub>0.2</sub> ) <sub>2</sub>	I+II	0.6	3.2	7.5
	I+II+III	1.4	9.3	18.4
Mo(Si <sub>0.9</sub> Ge <sub>0.1</sub> ) <sub>2</sub>	I+II	0.6	2.9	2.3
	I+II+III	2.6	13.9	19.4
Mo(Si <sub>0.75</sub> Ge <sub>0.25</sub> ) <sub>2</sub>	I+II	0.6	0.3	0.5
	I+II+III	2.9	8.3	8.3
(Mo <sub>0.71</sub> Nb <sub>0.29</sub> )Si <sub>2</sub>	I+II	1.0	2.8	7.5
	I+II+III	1.5	9.0	15.5
(Mo <sub>0.9</sub> Re <sub>0.1</sub> )Si <sub>2</sub>	I+II	0.6	0.8	2.7
	I+II+III	1.0	2.6	6.0
(Mo <sub>0.5</sub> Re <sub>0.5</sub> )Si <sub>2</sub>	I+II	0.7	3.3	1.9
	I+II+III	0.7	5.2	9.3



**TABLE 13 FOUR-POINT FLEXURE TEST RESULTS**

<b>Composition</b>	<b>Temp (°C)</b>	<b>UTS (MPa)</b>	<b>E (GPa)</b>	<b>ε (%)</b>	<b>DBTT (°C)</b>
<b>(Mo<sub>0.97</sub>Nb<sub>0.03</sub>)Si<sub>2</sub></b>	RT	146	236	0	
	1200	406	140	0.2	~1250
	1300	385	117	>1.85	
<b>(Mo<sub>0.93</sub>Nb<sub>0.07</sub>)Si<sub>2</sub></b>	RT	144	244	0	
	1200	284	144	0	
	1300	248	99	0.3	~1300
	1400	87	41	>2.6	
<b>(Mo<sub>0.85</sub>Nb<sub>0.15</sub>)Si<sub>2</sub></b>	RT	306	349	0	
	1300	422	83	0	~1350
	1400	252	76	>2.4	
<b>(Mo<sub>0.71</sub>Nb<sub>0.29</sub>)Si<sub>2</sub></b>	RT	142	204	0	
	1200	393	191	.1	~1250
	1300	309	137	>2.1	
<b>(Mo<sub>0.9</sub>Re<sub>0.1</sub>)Si<sub>2</sub></b>	RT	179	326	0	
	1300	332	207	0	~1350
	1400	254	81	>1.6	
<b>(Mo<sub>0.61</sub>Nb<sub>0.29</sub>Re<sub>0.1</sub>)Si<sub>2</sub></b>	RT	62	177	0	
	1300	230	153	0	~1350
	1400	119	147	>1.1	

**TABLE 14 THREE-POINT FLEXURE  $K_{IC}$  TEST RESULTS**

Composition		Temp (°C)		$K_{IC}$ (MPa·√m)
(Mo <sub>0.97</sub> Nb <sub>0.03</sub> )Si <sub>2</sub>		RT		0.9
		1200		0.4
		1300		1.0
(Mo <sub>0.93</sub> Nb <sub>0.07</sub> )Si <sub>2</sub>		RT		1.1
		1300		2.1
		1400		2.5
		1500		1.6
(Mo <sub>0.85</sub> Nb <sub>0.15</sub> )Si <sub>2</sub>		RT		2.7
		1300		3.5
		1400		2.2
(Mo <sub>0.71</sub> Nb <sub>0.29</sub> )Si <sub>2</sub>		RT		1.8
		1300		4.5
		1400		3.9
(Mo <sub>0.9</sub> Re <sub>0.1</sub> )Si <sub>2</sub>		RT		3.1
		1300		3.8
		1400		3.1
		1450		3.4
(Mo <sub>0.61</sub> Nb <sub>0.29</sub> Re <sub>0.1</sub> )Si <sub>2</sub>		RT		1.5
		1300		6.0
		1400		3.1

**TABLE 15 COMPRESSIVE YIELD STRESS TEST RESULTS**

		<b>0.1 % Yield Stress (MPa)</b>				
<b>Composition</b>		<b>1000°C</b>	<b>1100°C</b>	<b>1200°C</b>	<b>1300°C</b>	<b>1400°C</b>
<b>MoSi<sub>2</sub></b>		799	661	455	365	165
<b>(Mo<sub>0.97</sub>Nb<sub>0.03</sub>)Si<sub>2</sub></b>		924	731	469	309	162
<b>(Mo<sub>0.93</sub>Nb<sub>0.07</sub>)Si<sub>2</sub></b>		814	658	485	315	181
<b>(Mo<sub>0.85</sub>Nb<sub>0.15</sub>)Si<sub>2</sub></b>		1186	917	654	450	283
<b>(Mo<sub>0.71</sub>Nb<sub>0.29</sub>)Si<sub>2</sub></b>		1062	786	519	319	188
<b>(Mo<sub>0.9</sub>Re<sub>0.1</sub>)Si<sub>2</sub></b>		1234	758	450	318	181
<b>(Mo<sub>0.61</sub>Nb<sub>0.29</sub>Re<sub>0.1</sub>)Si<sub>2</sub></b>		1579	1065	580	261	134

TABLE 16 MINIMUM CREEP RATES AT 1000°C

Minimum Creep Rate (s <sup>-1</sup> )							
Stress (MPa)		1 Nb	2.5 Nb	5 Nb	9.5 Nb	3.3 Re	9.5Nb-3Re
84.5		8.0E-7				4.2E-7	
85.7				6.1E-7			2.8E-7
160					1.9E-6		
169		1.9E-6				1.4E-6	
171			1.4E-6	8.6E-7			1.1E-6
240					3.8E-6		
254		4.4E-6				4.1E-6	2.6E-6
257			4.8E-6	1.3E-6			
321					7.9E-6		
338		8.9E-6				1.9E-5	
343			1.3E-5	1.5E-6			4.5E-6
401					1.7E-5		
423		1.8E-5					
429			3.8E-5	3.0E-6			8.0E-6
481					4.3E-5		
507		3.5E-5					
514			1.2E-4	4.9E-6			1.5E-5
592		7.0E-5					
600				8.3E-6			3.4E-5
686				1.6E-5			
772				3.0E-5			
858				6.1E-5			

**TABLE 17 MINIMUM CREEP RATES AT 1200°C**

Minimum Creep Rate (s <sup>-1</sup> )						
Stress (MPa)	1 Nb	2.5 Nb	5 Nb	9.5 Nb	3.3 Re	9.5Nb-3Re
85	8.0E-7				4.2E-7	
86			6.1E-7			2.8E-7
160				1.9E-6		
169	1.9E-6				1.4E-6	
171		1.4E-6	8.6E-7			1.1E-6
240				3.8E-6		
254	4.4E-6				4.1E-6	2.6E-6
257		4.8E-6	1.3E-6			
321				7.9E-6		
338	8.9E-6				1.9E-5	
343		1.3E-5	1.5E-6			4.5E-6
401				1.7E-5		
423	1.8E-5					
429		3.8E-5	3.0E-6			8.0E-6
481				4.3E-5		
507	3.5E-5					
514		1.2E-4	4.9E-6			1.5E-5
592	7.0E-5					
600			8.3E-6			3.4E-5
686			1.6E-5			
772			3.0E-5			
858			6.1E-5			

**TABLE 18 MINIMUM CREEP RATES AT 1400°C**

Minimum Creep Rate (s <sup>-1</sup> )						
Stress (MPa)	1 Nb	2.5 Nb	5 Nb	9.5 Nb	3.3 Re	9.5Nb-3Re
16				1.2E-6		
17.2	1.9E-6	8.7E-6			4.7E-6	2.0E-6
32.1				2.9E-6		
34.2	5.5E-6	1.5E-5	1.0E-5		8.9E-6	7.6E-6
48.1				6.3E-6		
51.5	9.0E-6	2.2E-5			1.5E-5	1.5E-5
64.1				1.1E-5		
68.5	1.4E-5	2.0E-5	1.3E-5		2.2E-5	2.3E-5
80.2				1.3E-5		
85.8	1.8E-5				3.2E-5	3.2E-5
96.2				1.8E-5		
102.6	2.4E-5		1.6E-5		5.8E-4	4.3E-5
112.2				2.2E-5		
120	3.1E-5					5.4E-5
128.3				2.8E-5		
136.9	3.9E-5		1.6E-5			6.4E-5
154.4	4.8E-5					7.7E-5
171.1	5.7E-5		1.9E-5			9.0E-5
187.7						8.9E-5
204.8			2.4E-5			
238.9			3.2E-5			
273.1			4.4E-5			
307.2			5.8E-5			
341.3			8.1E-5			

TABLE 19 COMPRESSIVE CREEP DUCTILITY RESULTS

Composition	Creep Region of interest	Creep Ductility (%)		
		1000°C	1200°C	1400°C
(Mo <sub>0.97</sub> Nb <sub>0.03</sub> )Si <sub>2</sub>	I+II	3.9	8.7	21.2
	I+II+III	9.1	19.6	30.5
(Mo <sub>0.93</sub> Nb <sub>0.07</sub> )Si <sub>2</sub>	I+II	1.0	6.5	6.2
	I+II+III	1.4	11.0	9.1
(Mo <sub>0.85</sub> Nb <sub>0.15</sub> )Si <sub>2</sub>	I+II	1.6	8.2	18.3
	I+II+III	1.8	14.1	23.0
(Mo <sub>0.71</sub> Nb <sub>0.29</sub> )Si <sub>2</sub>	I+II	1.5	7.1	12.4
	I+II+III	2.7	9.5	16.3
(Mo <sub>0.9</sub> Re <sub>0.1</sub> )Si <sub>2</sub>	I+II	1.7	1.3	2.2
	I+II+III	2.9	6.5	5.9
(Mo <sub>0.61</sub> Nb <sub>0.29</sub> Re <sub>0.1</sub> )Si <sub>2</sub>	I+II	1.7	5.8	48.0
	I+II+III	2.0	9.3	56.7

**TABLE 20 ISOTHERMAL OXIDATION RESULTS (1400°C)**

Composition	Weight Change (mg/cm <sup>2</sup> )	
	20 hours	120 hours
Baseline MoSi <sub>2</sub>	+0.5*	+1.2**
(Mo <sub>0.97</sub> Nb <sub>0.03</sub> )Si <sub>2</sub>	+0.2	+0.1
(Mo <sub>0.93</sub> Nb <sub>0.07</sub> )Si <sub>2</sub>	+0.4	+0.3
(Mo <sub>0.85</sub> Nb <sub>0.15</sub> )Si <sub>2</sub>	+0.2	+0.4
(Mo <sub>0.71</sub> Nb <sub>0.29</sub> )Si <sub>2</sub>	-1.2	-1.1
(Mo <sub>0.9</sub> Re <sub>0.1</sub> )Si <sub>2</sub>	+0.3	+0.4
(Mo <sub>0.61</sub> Nb <sub>0.29</sub> Re <sub>0.1</sub> )Si <sub>2</sub>	+0.6	-0.2

\*22 hours

\*\*124 hours



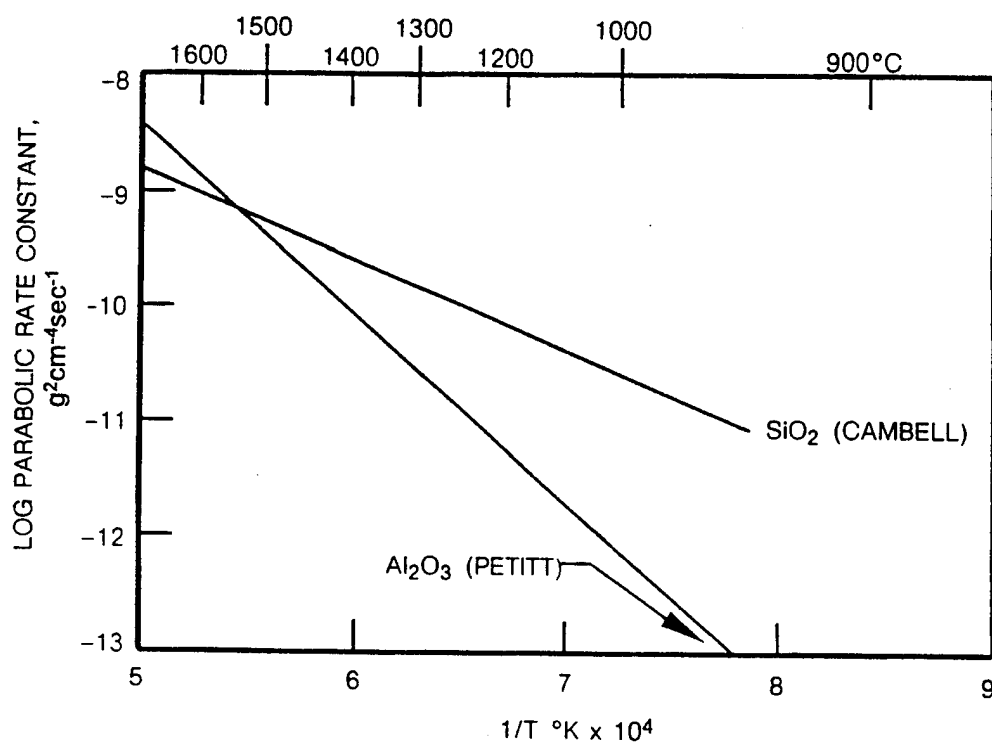


Fig. 1 Parabolic Rate Constants for  $\text{SiO}_2$  and  $\text{Al}_2\text{O}_3$

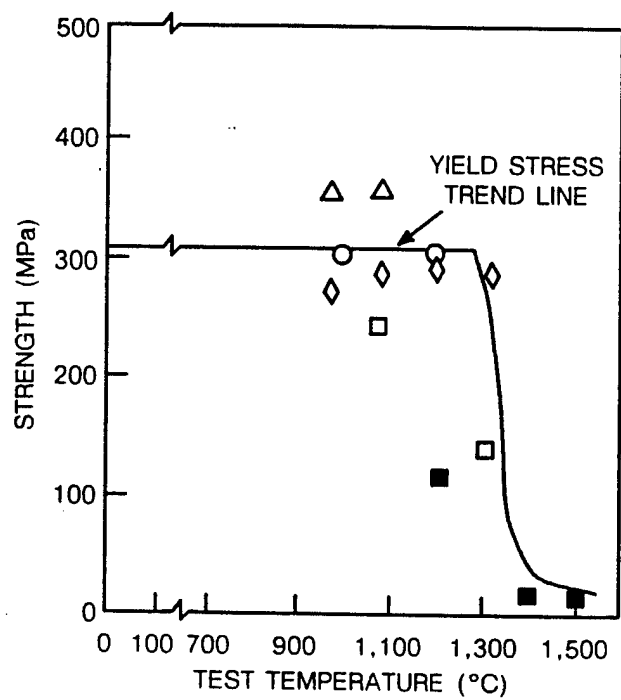


Fig. 2 Strength of  $\text{MoSi}_2$  (Ref. 4)

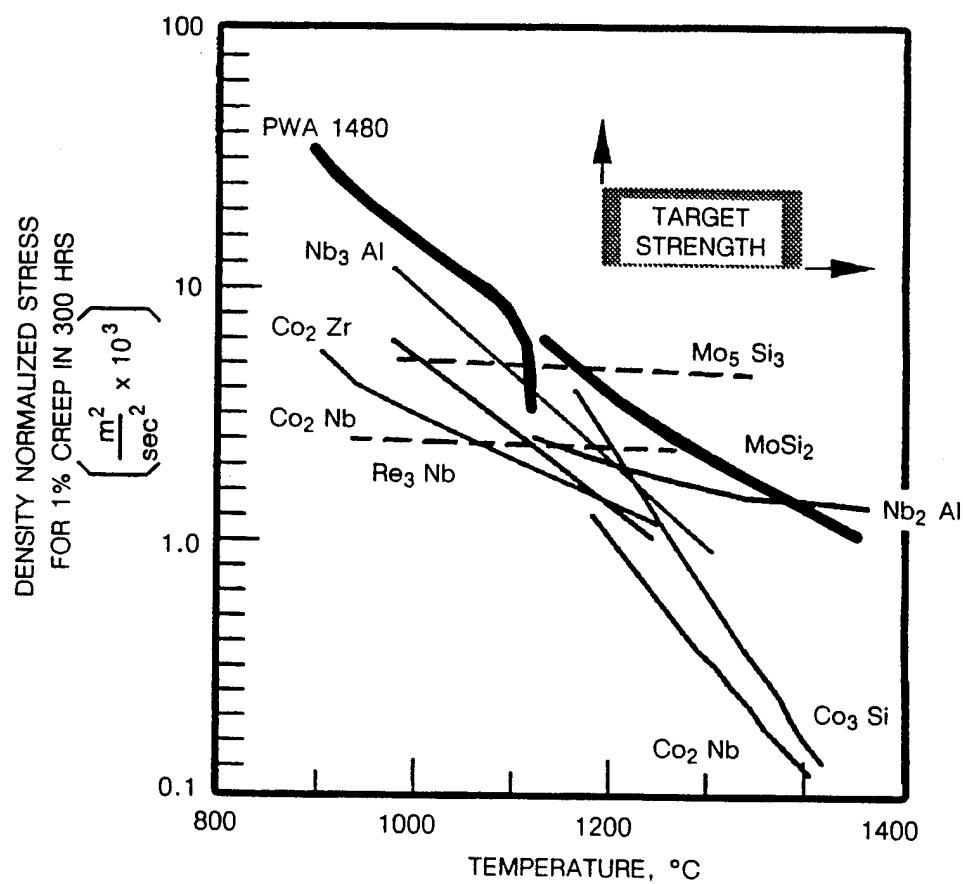


Fig. 3 Creep Strength of Various Intermetallics and Nickel-Based Superalloy PWA1480 (Ref. 6)

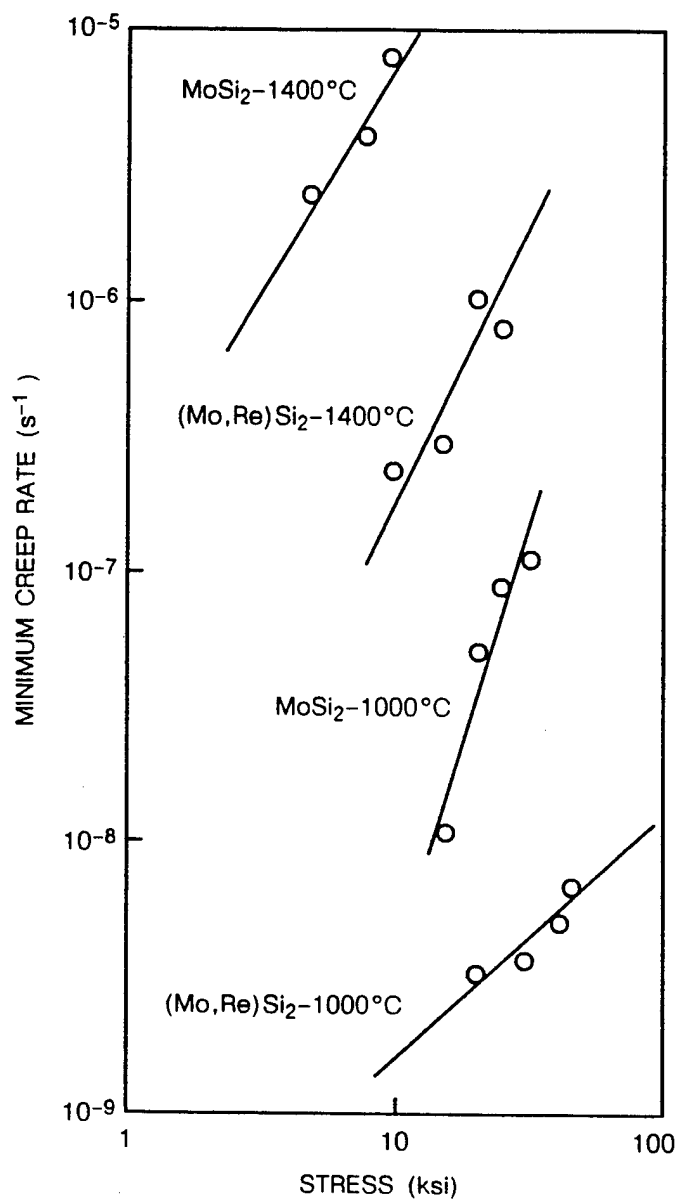


Fig. 4 Minimum Creep Rate of MoSi<sub>2</sub> and (Mo,Re) Si<sub>2</sub> (Ref. 6)

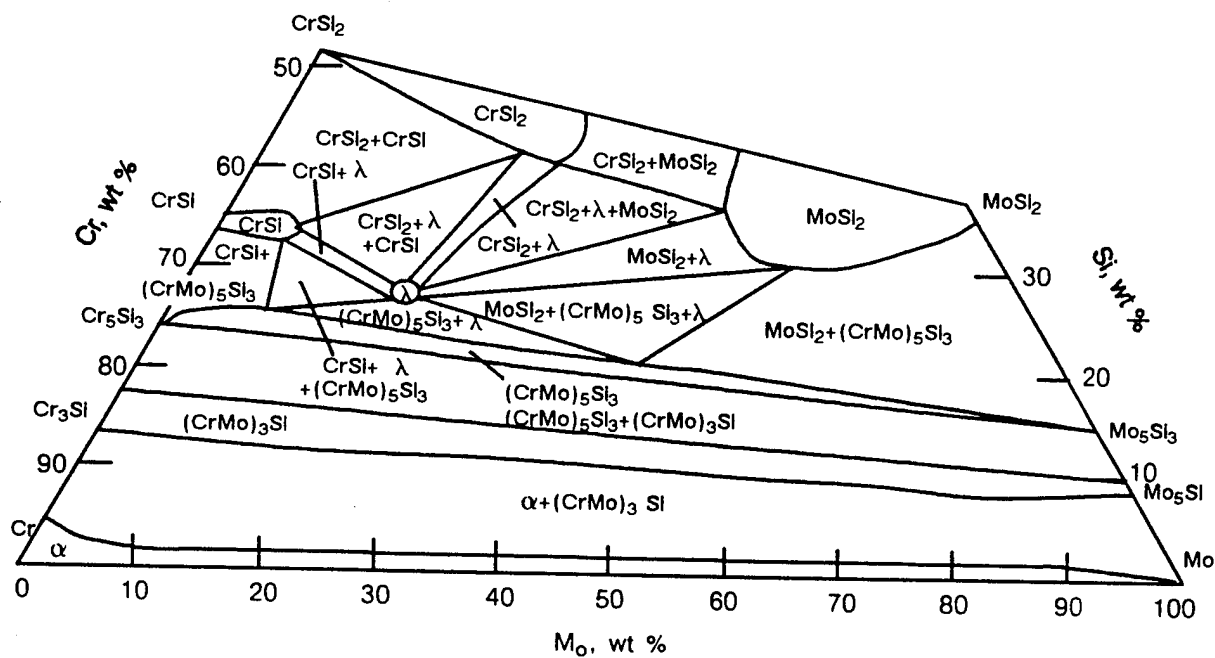
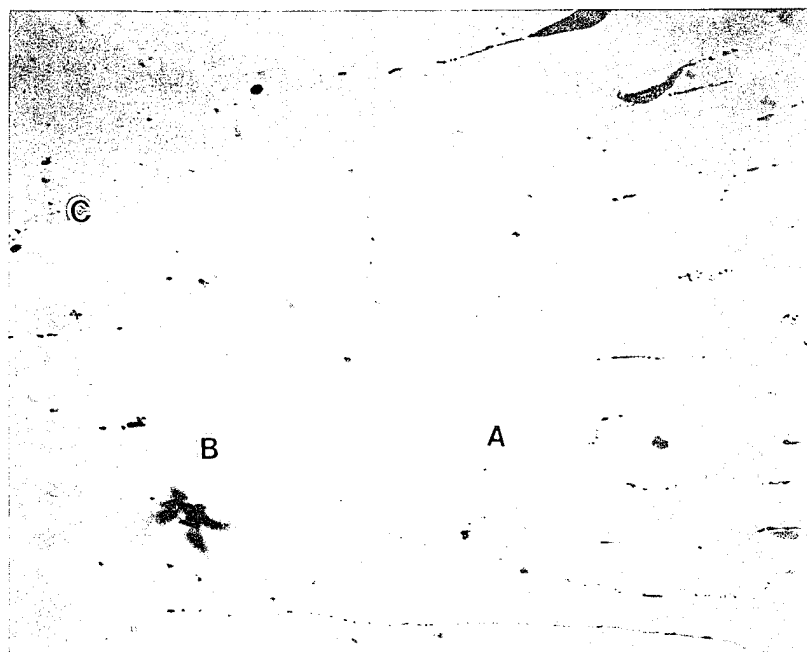


Fig. 5 Cr-Mo-Si Phase Diagram (Ref. 9)



100X

"A" Phase: 33.2 Mo - 58.1 Si - 8.6 Al

"B" Phase: 33.0 Mo - 63.8 Si - 3.2 Al

"C" Phase: 60.9 Mo - 38.6 Si - 0.4 Al

Figure 6 Backscatter Electron Image and Electron Probe Microanalysis of  $\text{MoSi}_2$  alloy with a nominal composition of 33.3 Mo - 61.7 Si - 5.0 Al (all in atomic %)



"X" Phase: 32.0 Mo - 34.7 Si - 33.3 Al

"Y" Phase: 18.8 Mo - 4.8 Si - 76.4 Al

"Z" Phase: 26.2 Mo - 2.6 Si - 71.2 Al

Figure 7 Backscatter Electron Image and Electron Probe Microanalysis of MoSi<sub>2</sub> alloy with a nominal composition of 33.3 Mo - 33.4 Si - 33.3 Al (all in atomic %)



100X

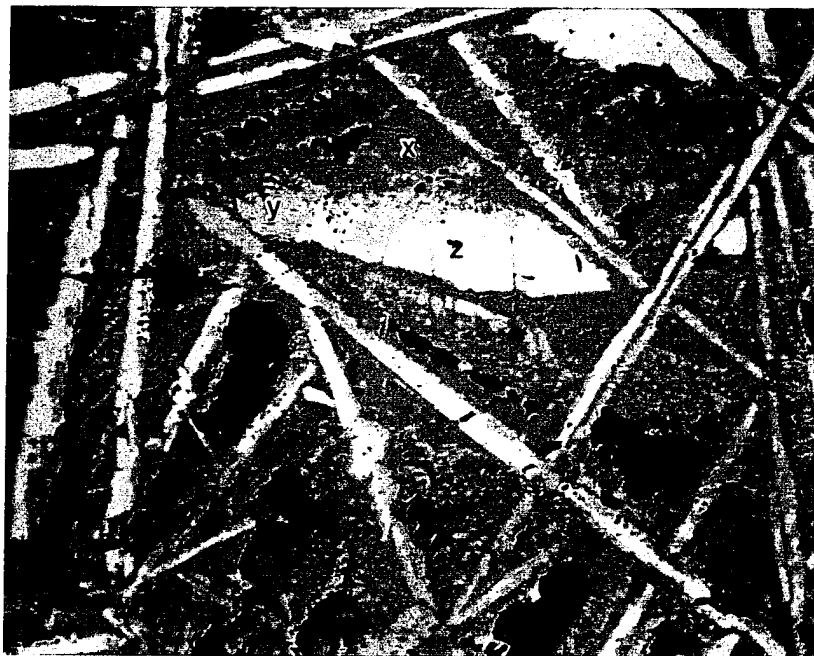
"A" Phase: 32.5 Mo - 25.9 Si - 41.6 Al

"B" Phase: 60.1 Mo - 31.6 Si - 8.3 Al

"C" Phase: 26.2 Mo - 1.7 Si - 72.1 Al

Figure 8 Backscatter Electron Image and Electron Probe Microanalysis of MoSi<sub>2</sub> alloy with a nominal composition of 33.3 Mo - 26.2 Si - 40.5 Al (all in atomic %)





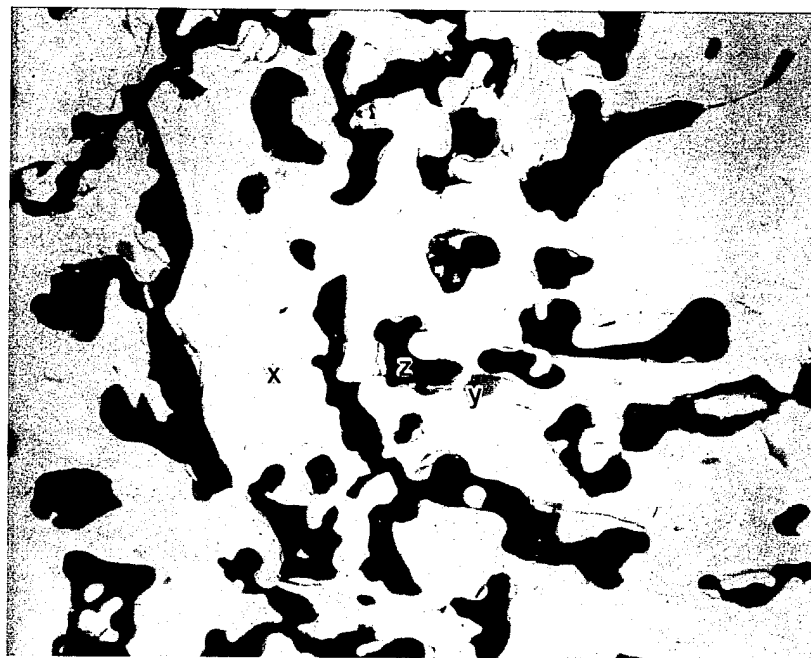
100X

"X" Phase: 32.9 Mo - 67.1 Si - 0.0 B

"Y" Phase: 32.9 Mo - 0.0 Si - 67.1 B

"Z" Phase: 50.7 Mo - 0.0 Si - 49.3 B

Figure 9 Backscatter Electron Image and Electron Probe Microanalysis of MoSi<sub>2</sub> alloy with a nominal composition of 33.3 Mo - 33.4 Si - 33.3 B (all in atomic %)



100X

"X" Phase: 32.6 Mo - 36.7 Si - 30.7 Ge

"Y" Phase: 34.7 Mo - 34.9 Si - 30.4 Ge

"Z" Phase: Epoxy Mounting Media

Figure 10 Backscatter Electron Image and Electron Probe Microanalysis of MoSi<sub>2</sub> alloy with a nominal composition of 33.3 Mo - 33.4 Si - 33.3 Ge (all in atomic %)



100X

"A" Phase: 0.0 Mo - 39.2 Hf - 60.8 Si

"B" Phase: 33.1 Mo - 0.05 Hf - 66.9 Si

"C" Phase: 0.2 Mo - 57.4 Hf - 42.4 Si

Figure 11 Backscatter Electron Image and Electron Probe Microanalysis of  $\text{MoSi}_2$  alloy with a nominal composition of 16.7 Mo - 16.6 Hf - 66.7 Si (all in atomic %)



100X

"a" Phase: 26.5 Mo - 6.7 Nb - 66.8 Si

"b" Phase: 31.5 Mo - 1.5 Nb - 67.0 Si

"c" Phase: 26.0 Mo - 6.8 Nb - 67.2 Si

"d" Phase: 4.0 Mo - 94.5 Nb - 1.5 Si

Figure 12 Backscatter Electron Image and Electron Probe Microanalysis of  $\text{MoSi}_2$  alloy with a nominal composition of 27.0 Mo - 6.3 Nb - 66.7 Si (all in atomic %)

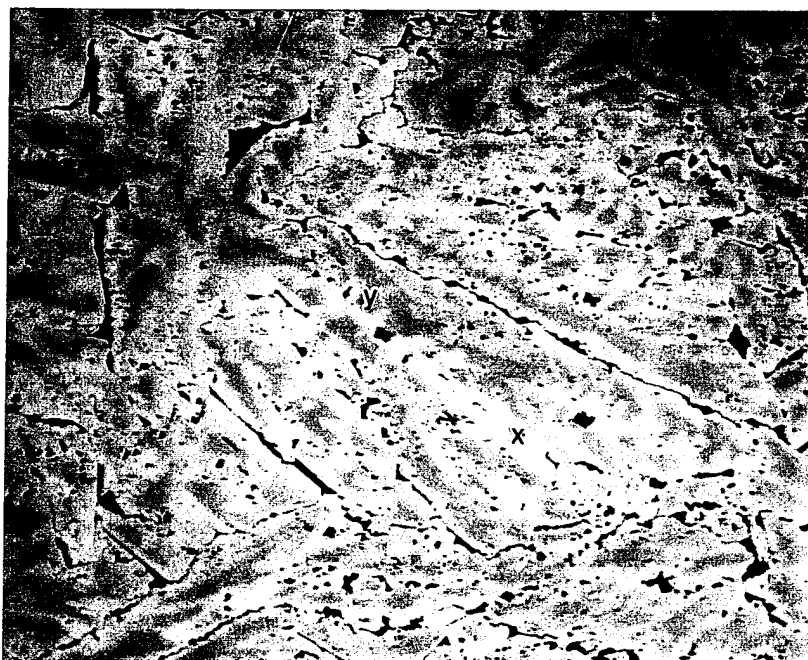


100X

"X" Phase: 16.7 Mo - 16.5 Nb - 66.7 Si

"Y" Phase: 28.9 Mo - 31.8 Nb - 39.3 Si

Figure 13 Backscatter Electron Image and Electron Probe Microanalysis of  $\text{MoSi}_2$  alloy with a nominal composition of 16.7 Mo - 16.6 Nb - 66.7 Si (all in atomic %)



100X

"X" Phase: 13.1 Mo - 18.7 Re - 68.2 Si

"Y" Phase: 20.8 Mo - 11.1 Re - 68.0 Si

Figure 14 Backscatter Electron Image and Electron Probe Microanalysis of  $\text{MoSi}_2$  alloy with a nominal composition of 16.7 Mo - 16.6 Re - 66.7 Si (all in atomic %)

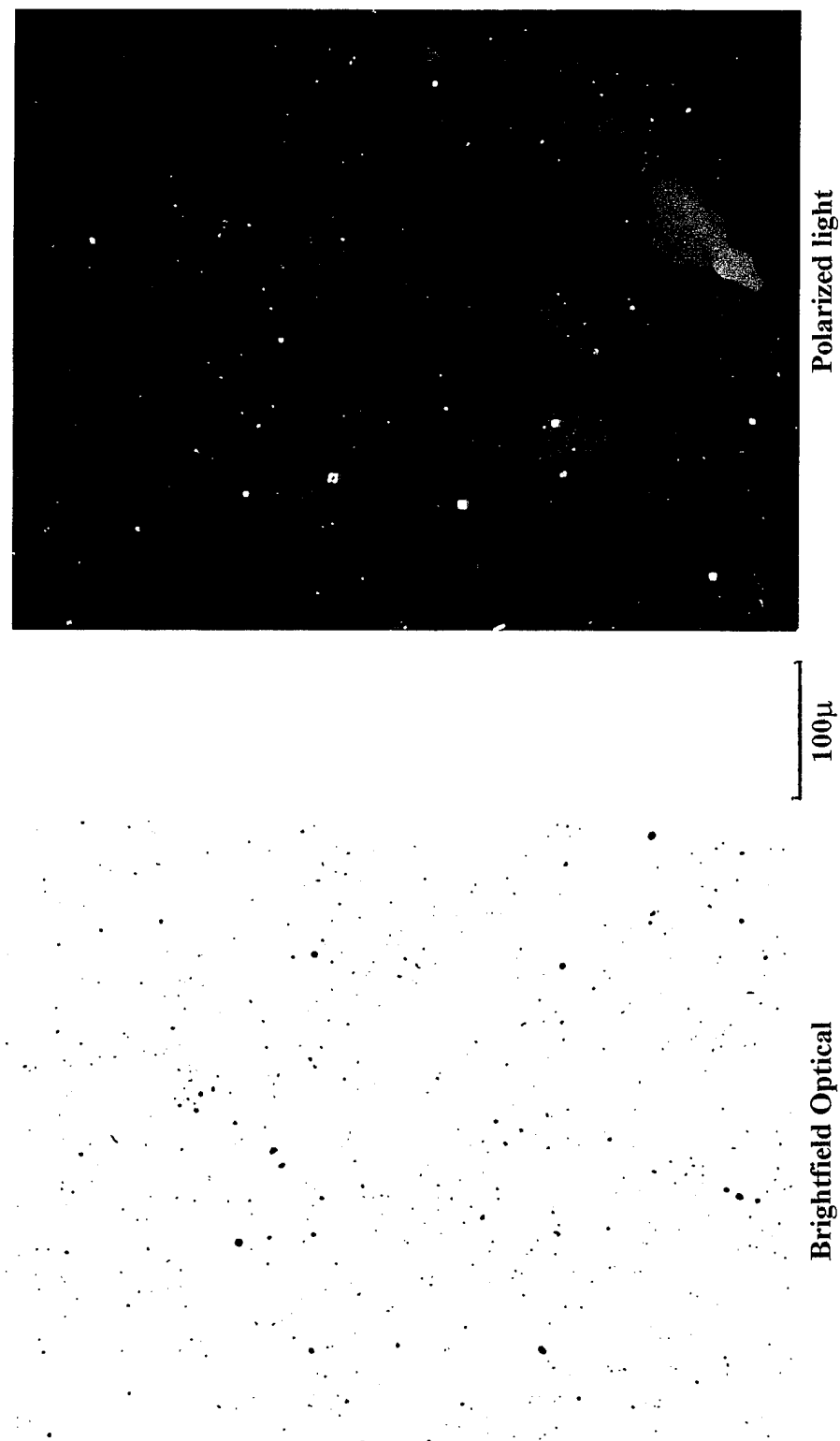


**Fig. 6 Microstructure of MoSi<sub>2</sub> Prepared by Powder Metallurgy**

Fig. 16 COMPRESSIVE YIELD STRESS

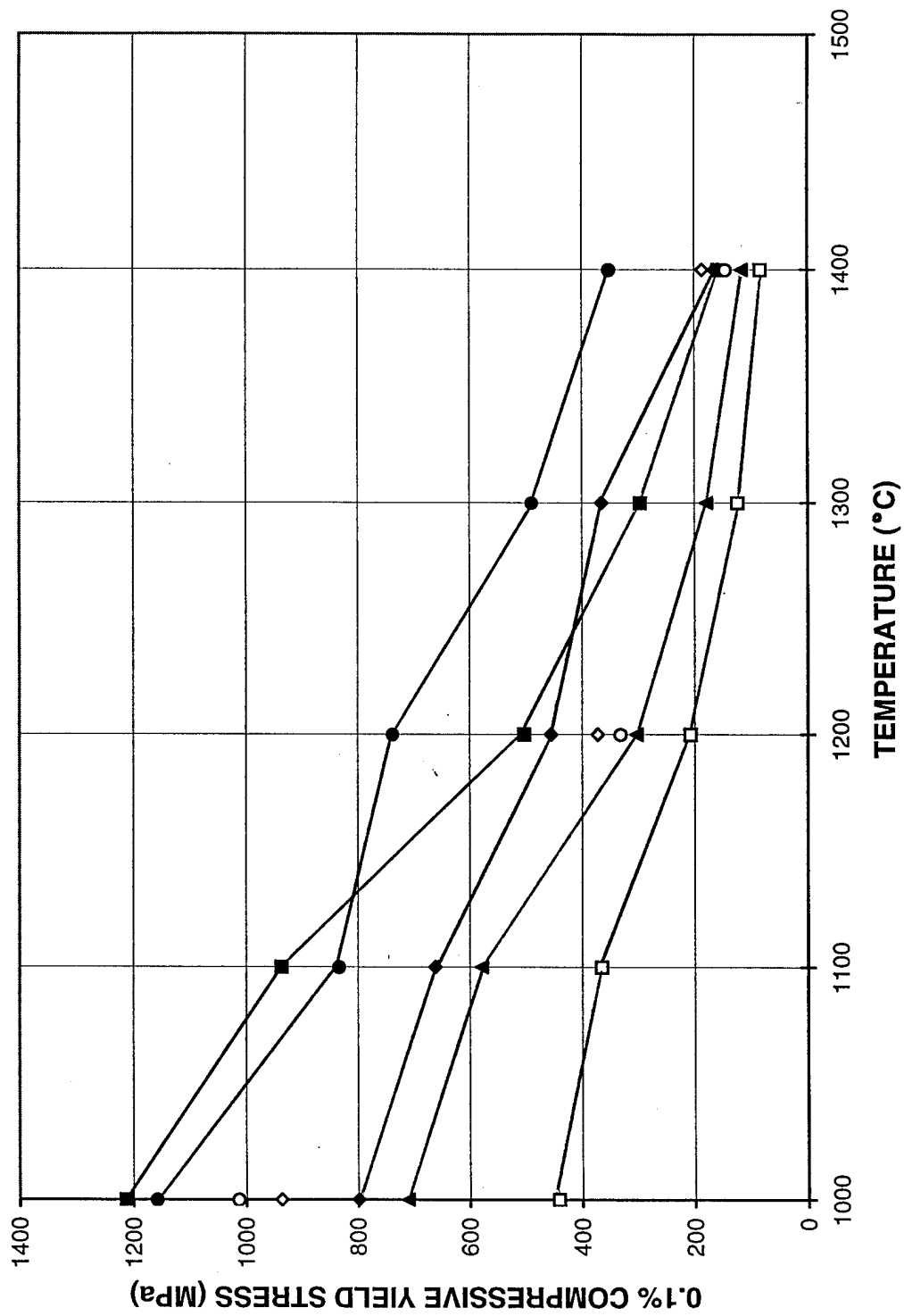




Fig. 17 1000°C COMPRESSIVE CREEP

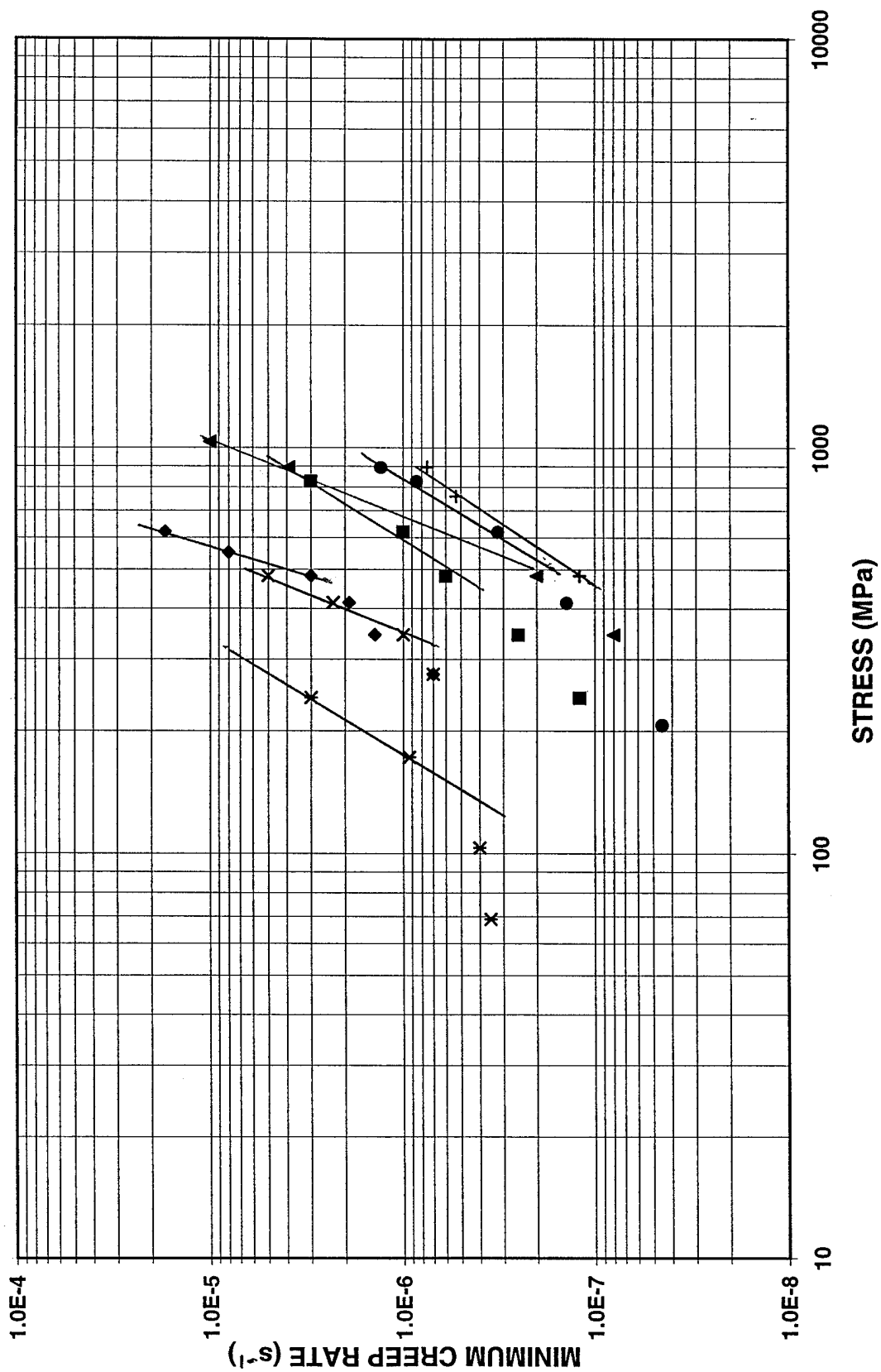


Fig. 18 1200°C COMPRESSIVE CREEP

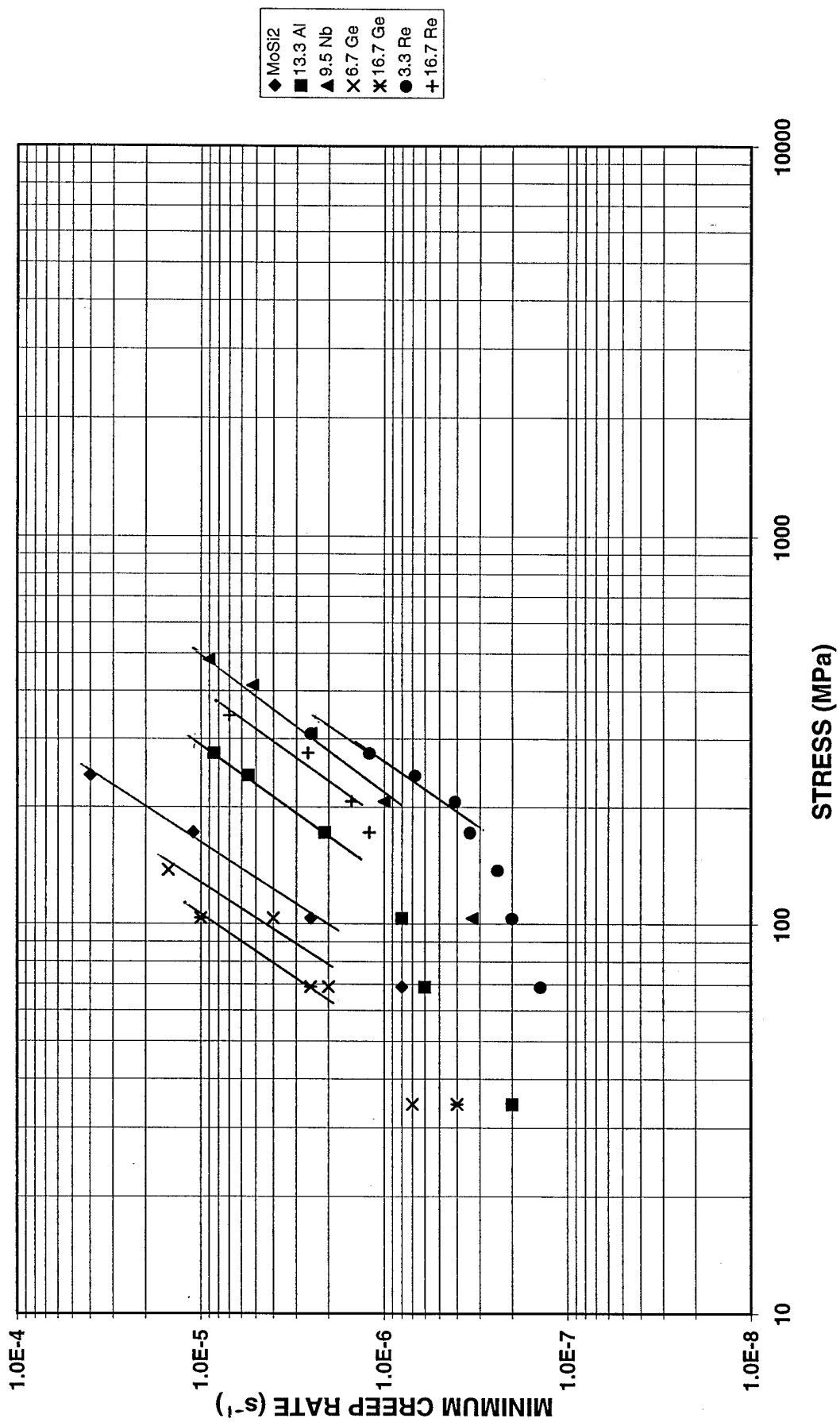


Fig. 19 1400°C COMPRESSIVE CREEP

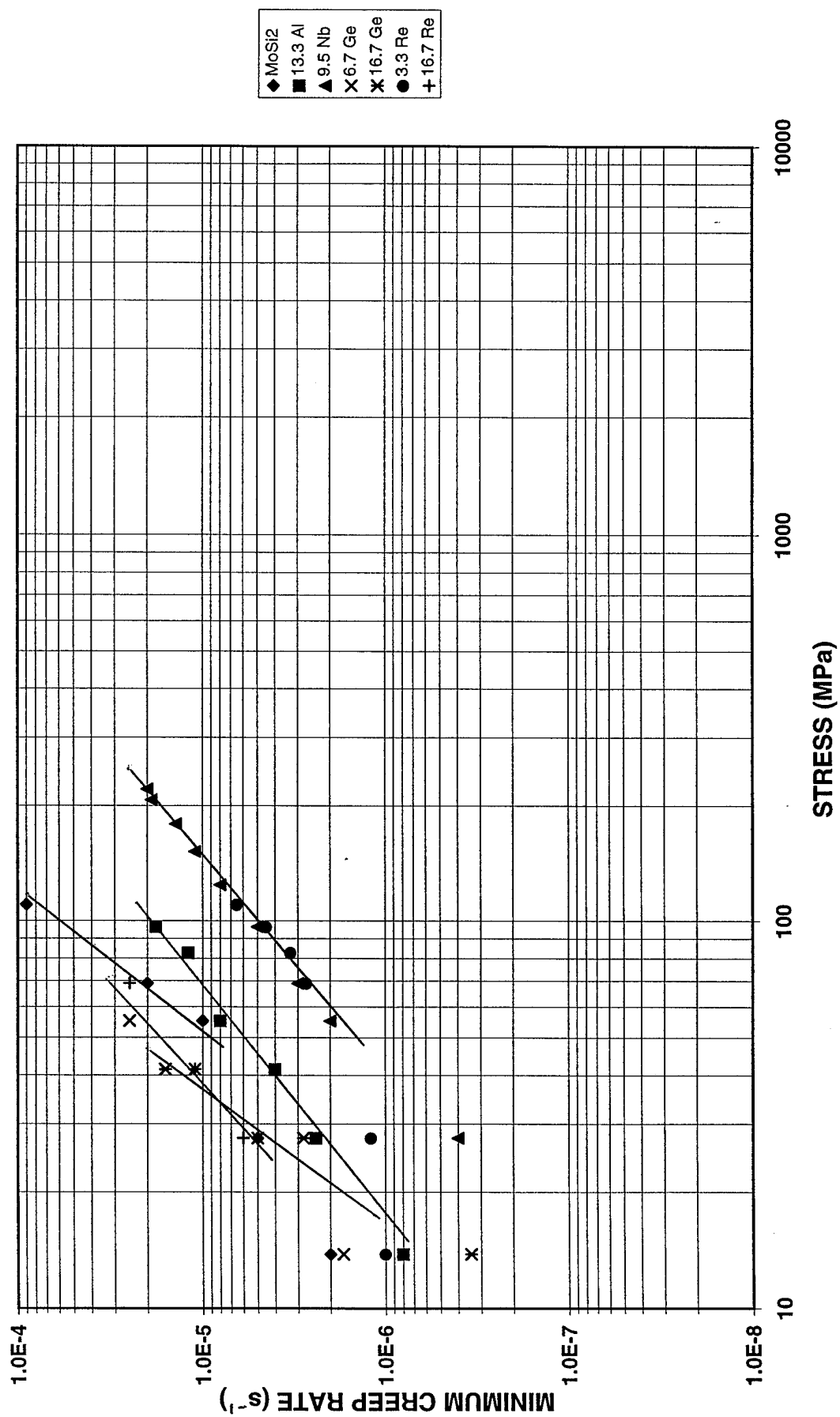


Fig 20 COMPRESSIVE YIELD STRESS

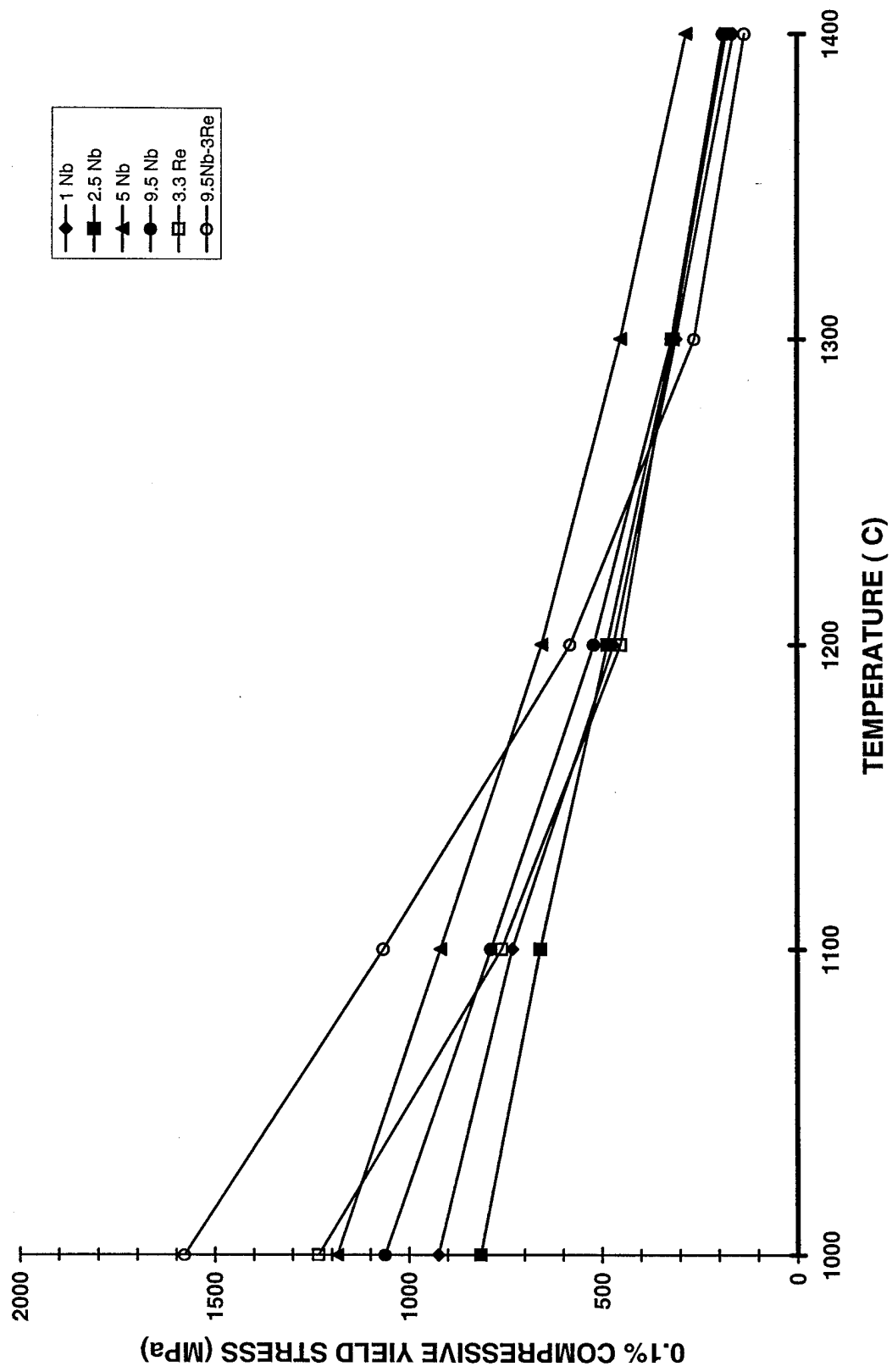


Fig. 21 1000°C COMPRESSIVE CREEP

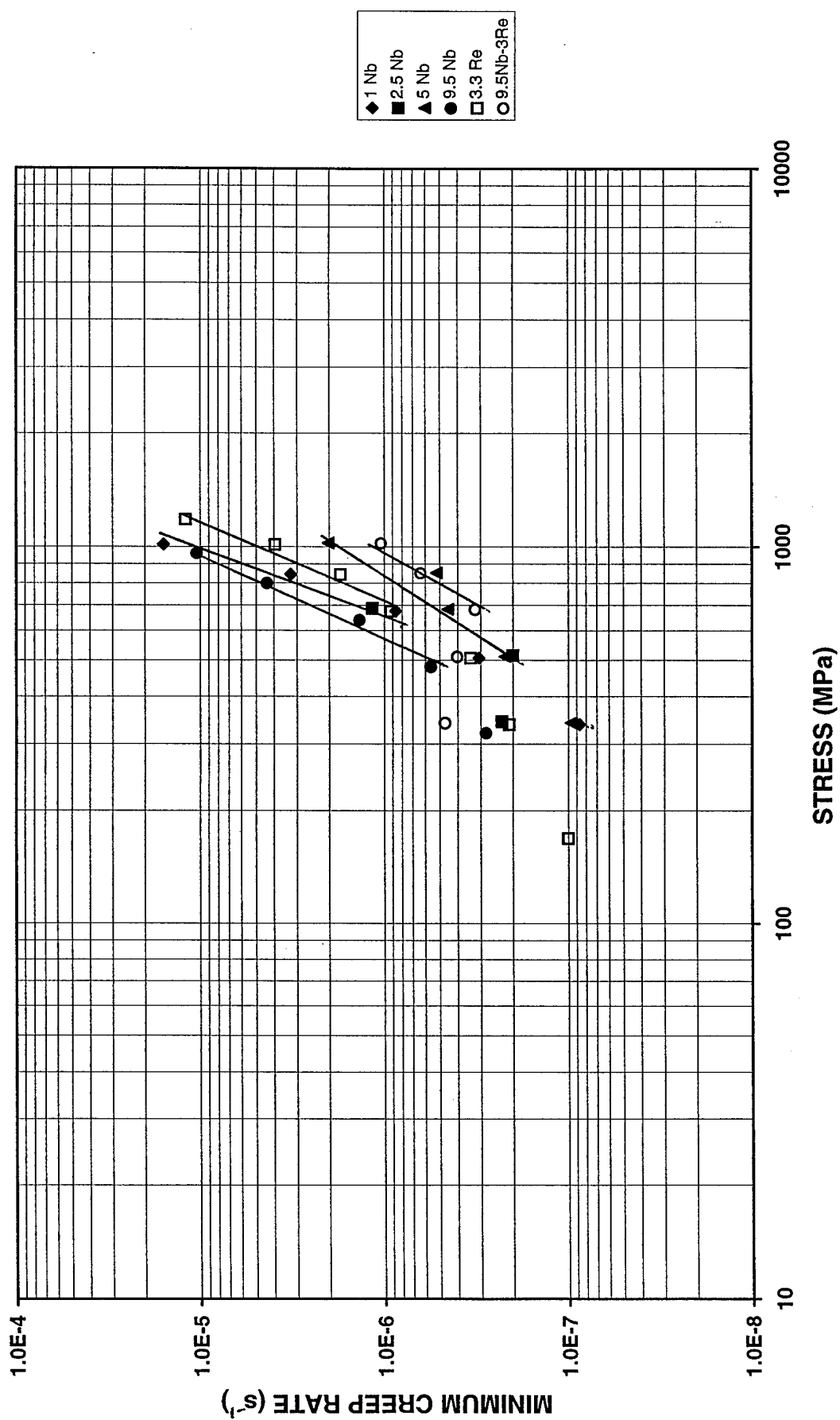


Fig. 22 1200°C COMPRESSIVE CREEP

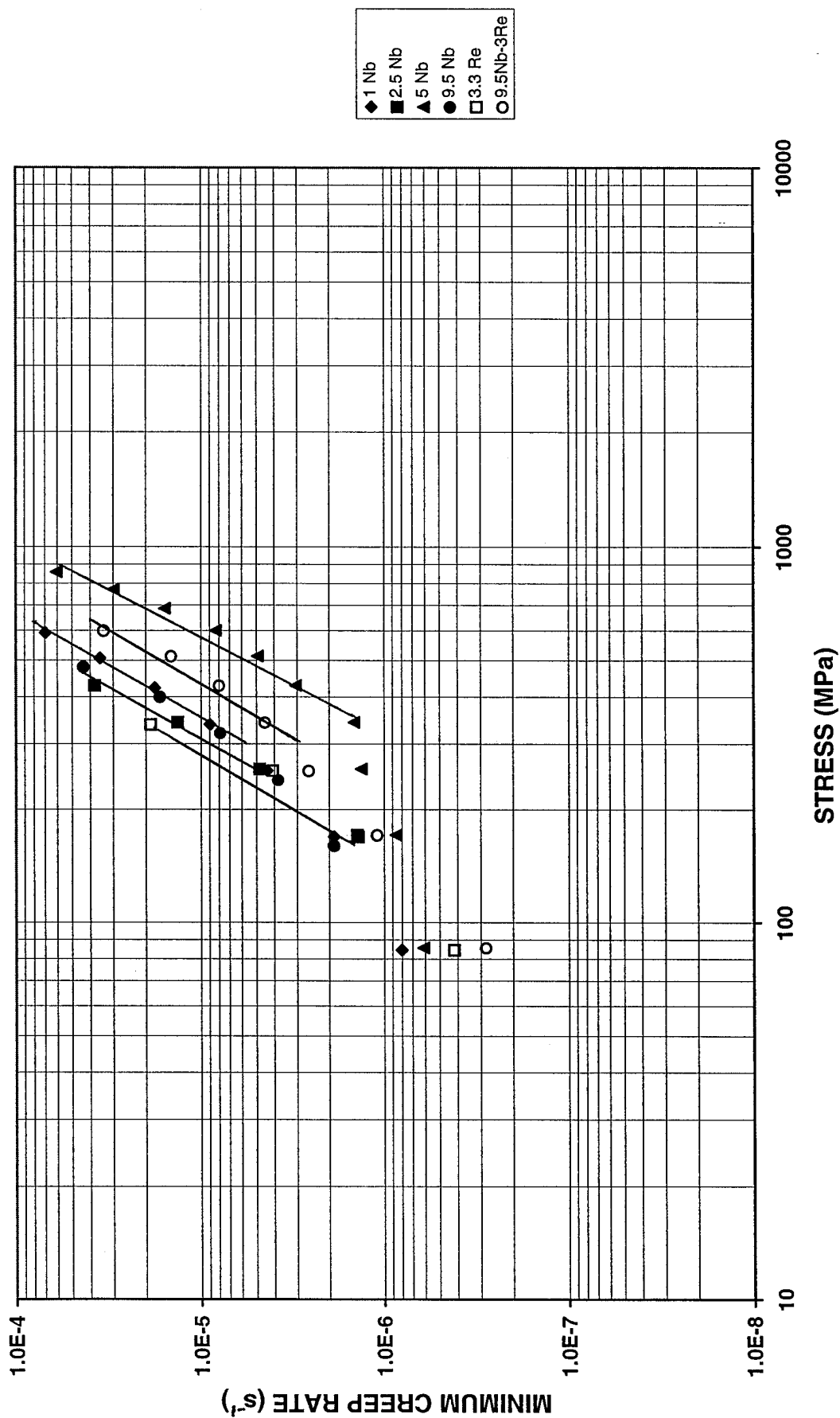
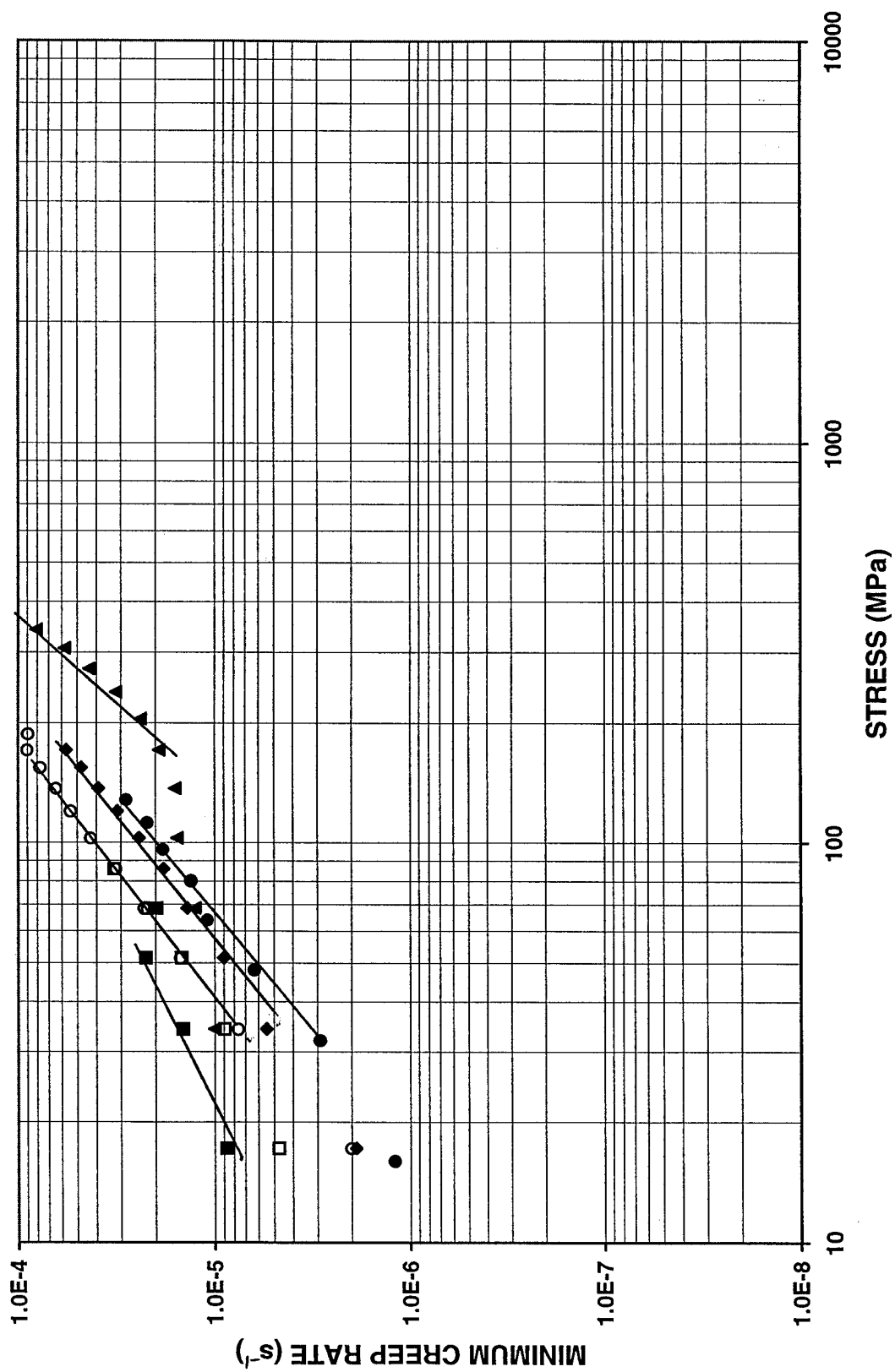


Fig. 23 1400°C COMPRESSIVE CREEP



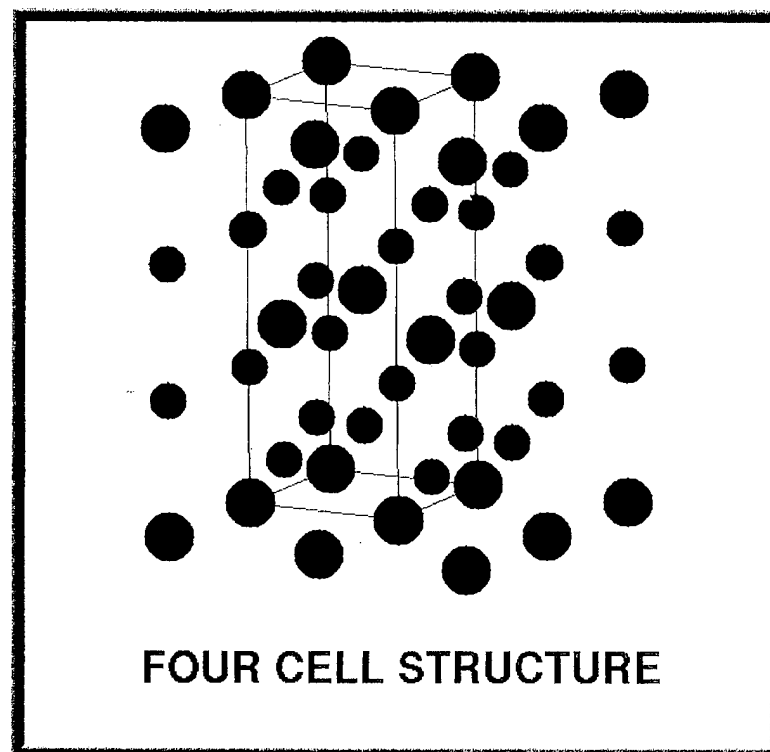
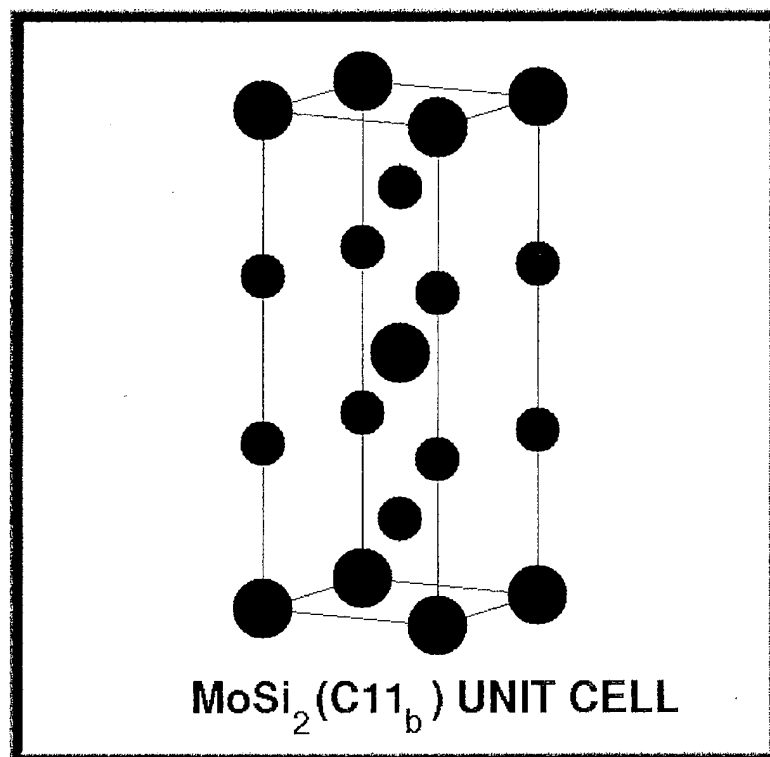
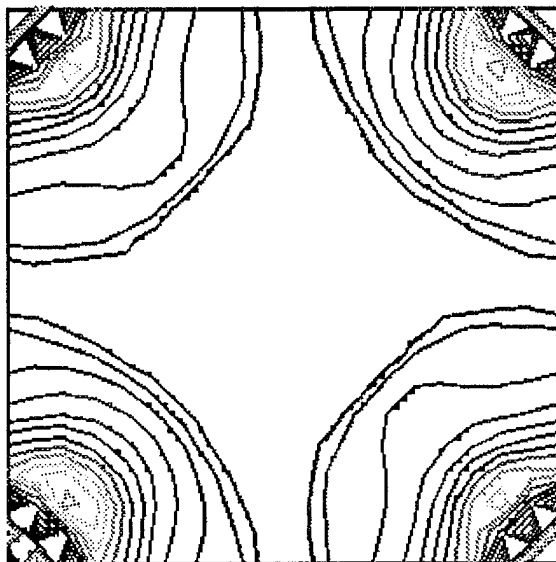


Fig. 24 Visualization of  $\text{MoSi}_2$  Structure

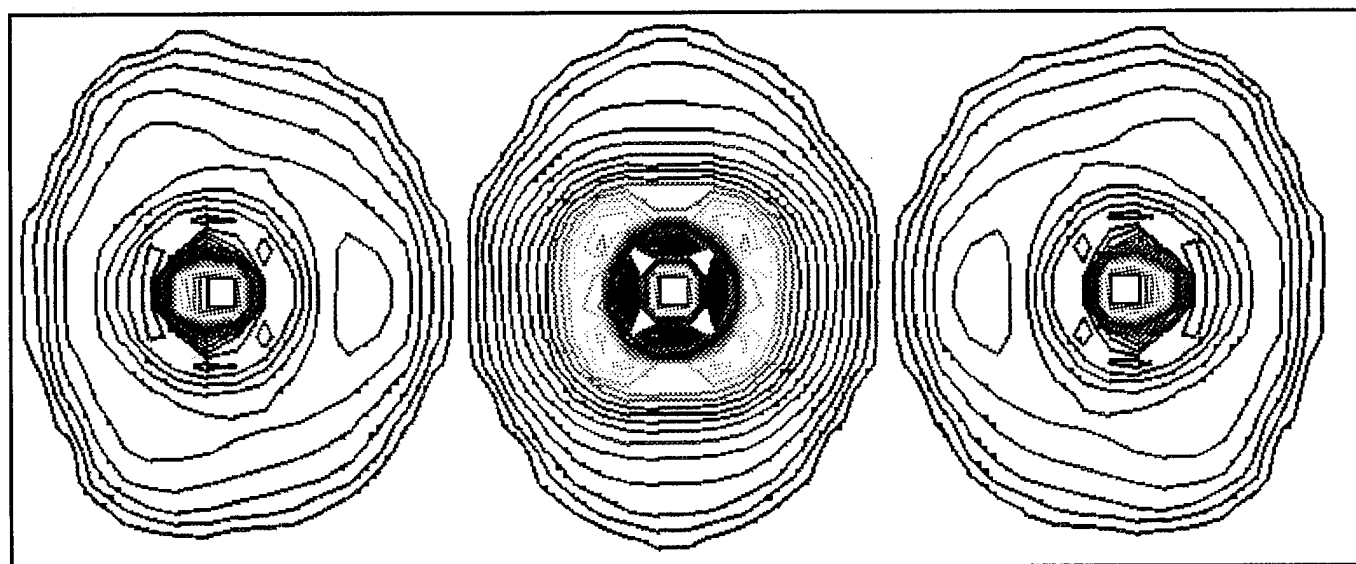
91-10-30-4





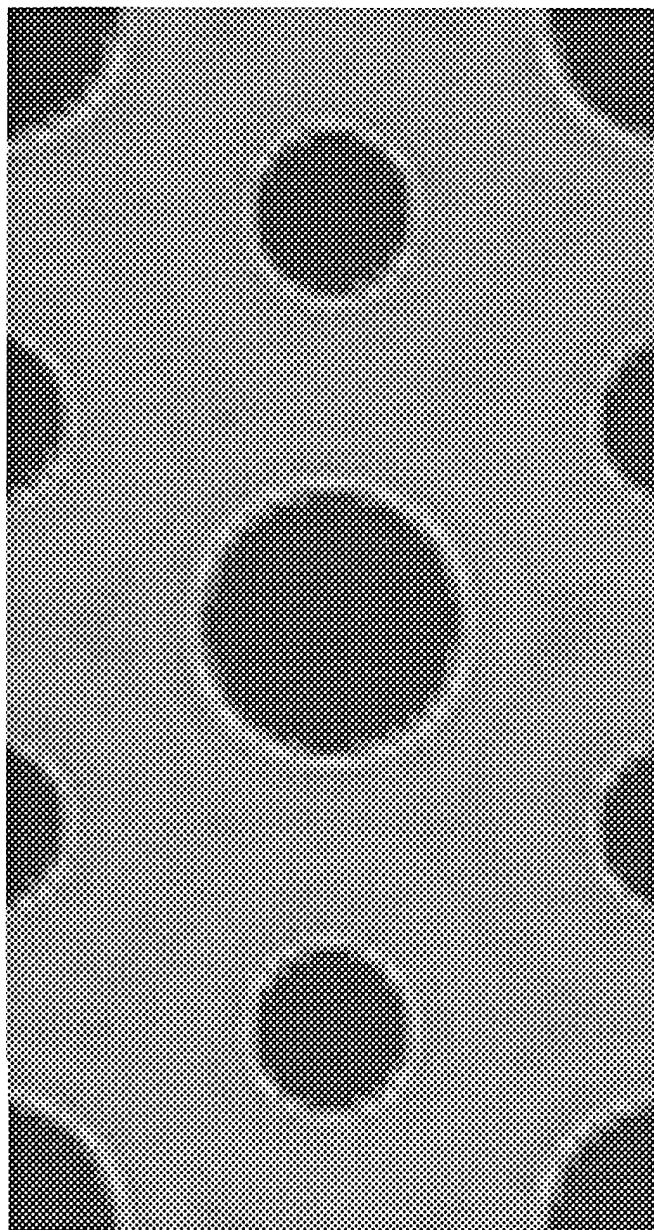
Case B  
 $\text{MoSi}_2(2) \quad (001)$

Fig. 25  $\text{MoSi}_2$  (001) Charge Density Contours

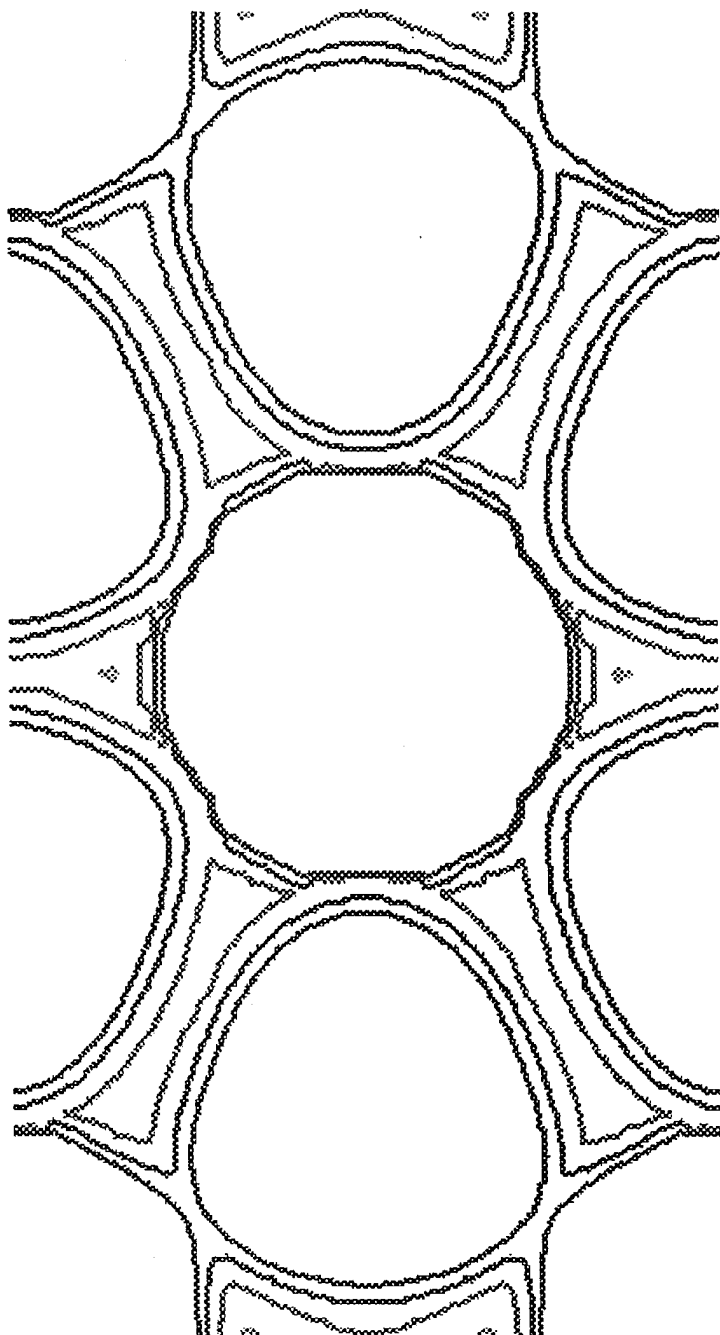


Case B  
MoSi<sub>2</sub>(2) (200)

Fig. 26 MoSi<sub>2</sub> (200) Charge Density Contours

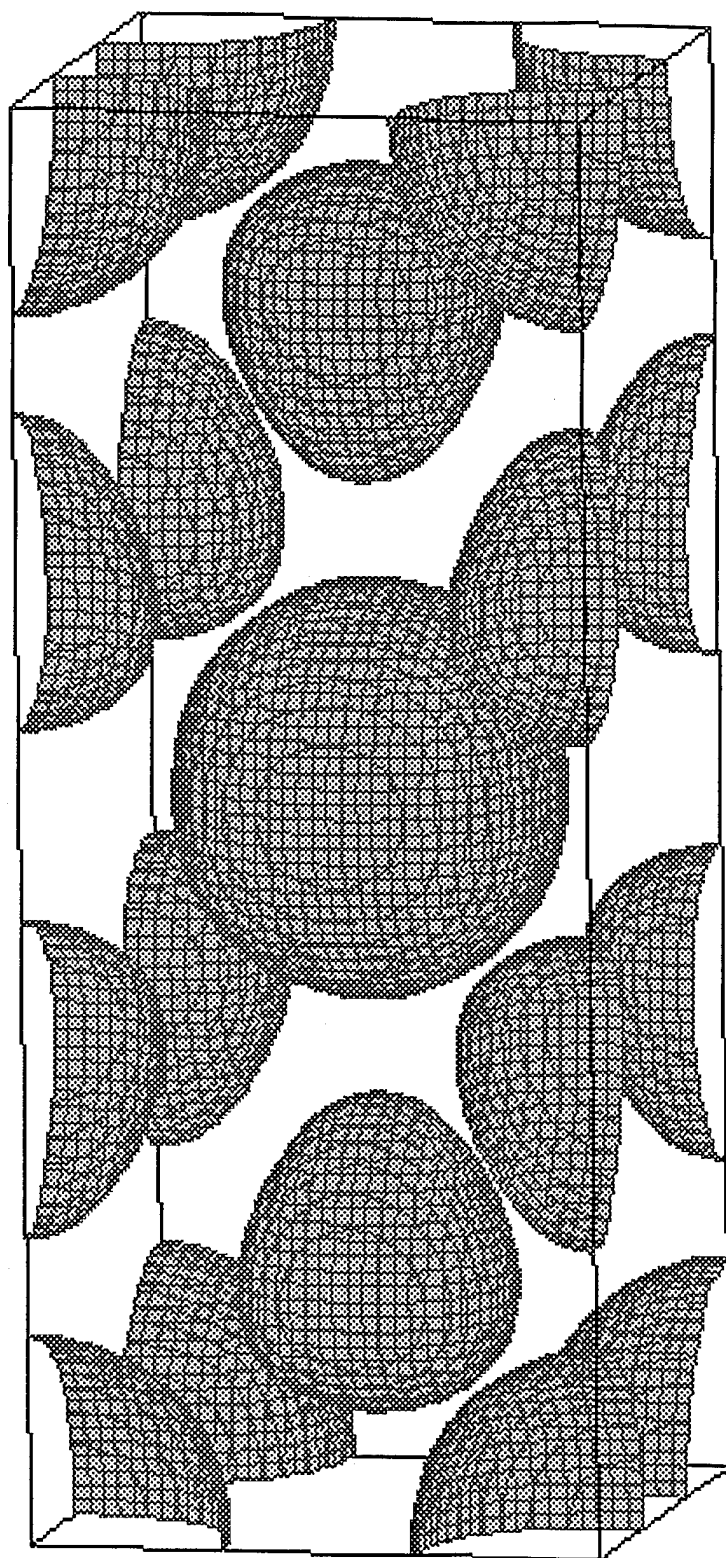


MoSi<sub>2</sub> (110) Charge Density



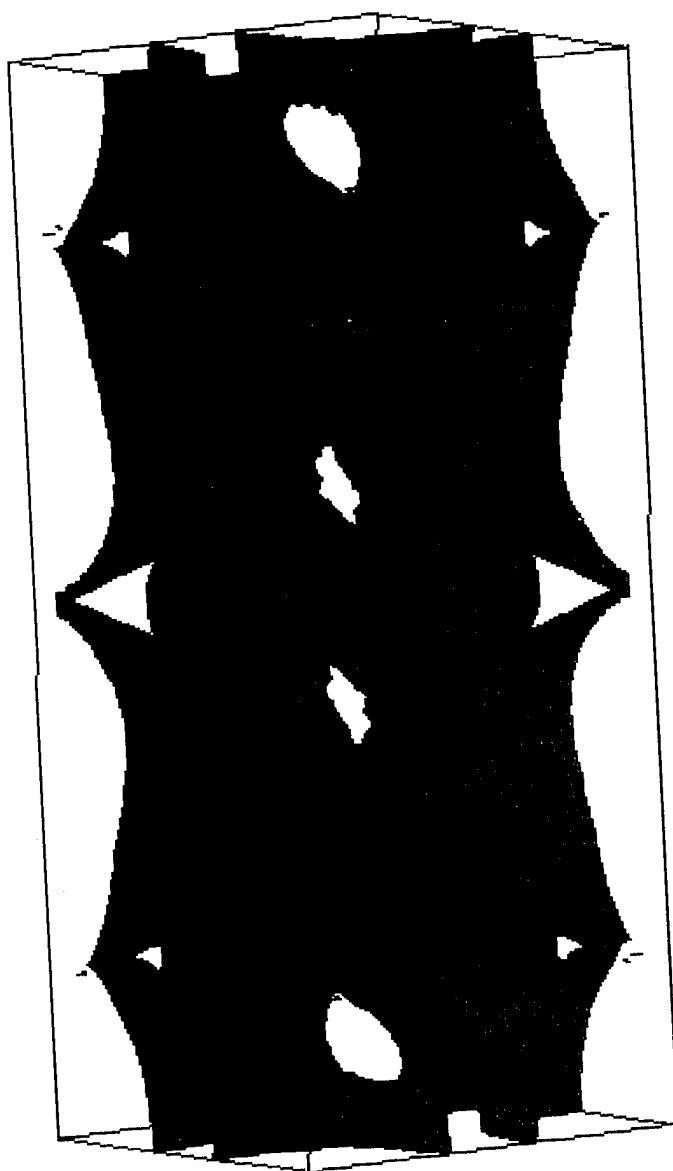
**MoSi<sub>2</sub> (110) Charge Density**

Fig. 28



## MoSi(2) Charge Density

Fig. 29



**MoSi<sub>2</sub> Charge Density**

Fig. 30